ELSEVIER

Journal of Fluids and Structures 23 (2007) 605–631

JOURNAL OF FLUIDS AND STRUCTURES

www.elsevier.com/locate/jfs

Time domain analysis of second-order wave diffraction by an array of vertical cylinders

C.Z. Wang, G.X. Wu*

Department of Mechanical Engineering, University College London, Torrington Place, London WC1E 7JE, UK

Received 27 September 2005; accepted 22 October 2006
Available online 12 January 2007

Abstract

A time domain method is employed to analyze interactions of water waves and a group or an array of cylinders. The nonlinear free-surface boundary conditions are satisfied based on the perturbation method up to the second order. The first- and second-order velocity potential problems at each time step are solved through a finite element method (FEM). The mesh required is generated based on a 2-D unstructured grid on a horizontal plane and its extension in the vertical direction. The matrix equation of the FEM is solved through an iteration and the initial solution is obtained from the result at the previous time step. The radiation condition is imposed through a combination of the damping zone method and the Sommerfeld–Orlanski equation. Results for various configurations, including two cylinders, four cylinders, an array of 10 cylinders and two arrays of eight cylinders are provided to show the effect of the interaction and their behaviour near the trapped mode.

Keywords: Finite element method; Unstructured mesh; Second-order wave diffraction; Time domain; An array of cylinders

1. Introduction

There has been extensive research into the second-order wave radiation and diffraction problems since the work of Lighthill (1979) and Molin (1979). They showed that the second-order force could be obtained through a fictitious radiation potential and the direct solution of the second-order potential itself was not be required. The method was extended by Eatock Taylor et al. (1989) to obtain the pressure on the body surface. They introduced a potential whose normal derivative is unit on the element where the pressure was evaluated and zero everywhere else. For the two-dimensional (2-D) problem, the method needs to be modified because the diffracted wave does not decay at infinity. As a result, the nonhomogeneous term in the free-surface boundary condition for the second-order potential tends to an oscillatory function and the equation derived by Lighthill (1979) and Molin (1979) will have a contribution from infinity (Wu and Eatock Taylor, 1990). Other extensions include that by Wu (1991) who obtained the second-order wave reflection and transmission at infinity in 2-D through introducing a different kind of fictitious function. The applications of this indirect method together with the direct solution method can be found in many publications, which include those by Molin and Marion (1986), Eatock Taylor and Hung (1987), Vada (1987), Abul-Azm and Williams (1988), Kim and Yue (1989), Chau (1989) and Chau and Eatock Taylor (1992).

*Corresponding author. Tel.: +44 20 76793870; fax: +44 20 73880180.
E-mail address: gx_wu@meng.ucl.ac.uk (G.X. Wu).

0889-9746/$ - see front matter
doi:10.1016/j.jfluidstructs.2006.10.008

One of the interesting problems in body/wave interactions is an array of vertical cylinders in an incoming wave. This configuration has a wide range of applications, such as bridges and floating airports. Maniar and Newman (1997) considered the linear diffraction by an array of 101 cylinders. They found that when the wavenumber was close to the trapped mode (Ursell, 1951), a very large hydrodynamic force could arise on the cylinders in the middle. Evans and Porter (1997a) also showed that a very large force could occur for a small number of cylinders, such as four, especially when they were quite close to each other. Malenica et al. (1999) further showed that similar behaviour could occur for the second-order result. The wavenumber for the first-order problem chosen by them was far away from the trapped mode and the linear result did not exhibit any unusual behaviour. The corresponding wavenumber for the second-order problem was, however, quite near the trapped mode. As a result, some of the second-order results were found to be abnormally large. Other investigations on an array of cylinders include those by Kashiwagi and Ohwatari (2002) and Ohl et al. (2001).

The work mentioned above is all based on the frequency domain method. There is some work on the time domain method, such as the theory of ship motions presented by Pawlovski (1992). The present paper is to use the time domain method to analyse the first- and second-order wave diffraction by a group or an array of cylinders. One of the advantages of the time domain method over the traditional frequency domain method is that it can capture more easily the transient effect if the motion is not periodic. Compared with the fully nonlinear theory, the domain in the perturbation method is fixed and therefore the solution procedure can be more efficient.

The time domain problem is usually solved by the boundary element method (BEM) through two schemes. The first one is to use a Green function which satisfies the free surface boundary condition. As a result, the differential equation can be converted into an integral equation. A typical example of this is the work by Beck and Liapis (1987). Unlike the frequency domain method, however, the integral equation contains a term of convolution which includes all the information prior to the current instant, or the memory effect. As time progresses, the memory effect can become too big for practical computation. The other scheme in the time domain method is to use the Rankine source. The Green function in this case does not satisfy the free surface boundary condition and a source distribution is required on the free surface. Typical examples of this scheme include those by Isaacson and Cheung (1990, 1991, 1992) on the second-order wave diffraction problems by a single cylinder. The advantage of the Rankine source method is that it removes the explicit memory effect from the equation. Its disadvantage is that it requires sources all over the free surface. As the matrix is fully populated, the storage requirement can also be very big. In the present work, we use the finite element method (FEM). As shown by Wu and Eatock Taylor (1995), even though the FEM has more unknowns, it has a smaller memory requirement because its matrix is banded. For this reason, it has been widely used in a variety of fully nonlinear problems in the time domain (Wu et al., 1998; Ma et al., 2001a, b; Hu et al., 2002; Wu and Hu, 2004; Wang and Wu, 2006) and is found to be very effective.

Simulation based on the FEM is made first for two cylinders to investigate the effect of the interaction through the comparison with the single cylinder case. Numerical results are provided for both the wave elevation and the force. Simulation is then made for four cylinders, and for both bottom mounted and truncated cylinders. The effect of the trapped mode on the first- and the second-order results is investigated. Simulation is also made for an array of 10 cylinders in a line and eight cylinders in two lines.

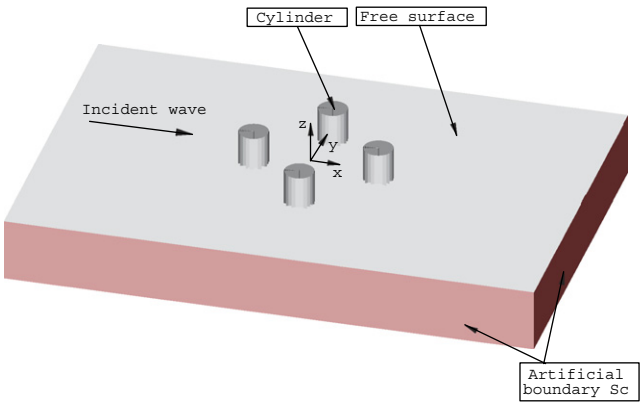

Fig. 1. A sketch of the problem.

2. Mathematical formulation

We consider the second-order wave diffraction problem by a group or an array of cylinders. As shown in Fig. 1, a right-handed Cartesian coordinate system $oxyz$ is defined, in which x and y are measured horizontally and z points vertically upwards from the still water level. The cylinder surface is denoted by S_b and its unit normal vector directed outward from the fluid region is denoted by $\vec{n} = (n_x, n_y, n_z)$. The seabed is assumed horizontal along the plane $z = -h$. Let t denote time and η be the elevation of the free surface S_f relative to the still water level. When the fluid is assumed incompressible and inviscid, and the flow irrotational, the fluid motion can be described by a velocity potential ϕ which satisfies the Laplace equation within the fluid domain Ω_f.

$$\nabla^2\phi = 0 \quad \text{in } \Omega_f \tag{1}$$

and is subject to the following boundary conditions:

$$\frac{\partial\phi}{\partial z} - \frac{\partial\eta}{\partial t} - \frac{\partial\phi}{\partial x}\frac{\partial\eta}{\partial x} - \frac{\partial\phi}{\partial y}\frac{\partial\eta}{\partial y} = 0 \quad \text{on } S_f, \tag{2}$$

$$\frac{\partial\phi}{\partial t} + g\eta + \frac{1}{2}|\nabla\phi|^2 = 0 \quad \text{on } S_f, \tag{3}$$

$$\frac{\partial\phi}{\partial n} = 0 \quad \text{on } S_b, \tag{4}$$

$$\frac{\partial\phi}{\partial n} = 0 \quad \text{on } z = -h, \tag{5}$$

where g is the acceleration due to gravity. In addition, the potential satisfies the radiation condition which is imposed through a suitable numerical procedure applied on a control surface S_c located at some distance away from the body as shown in Fig. 1.

Based on the second-order theory for the weakly nonlinear problem, Eqs. (2) and (3) can be satisfied on the still water surface through the Taylor expansion

$$\left(\frac{\partial\phi}{\partial z} - \frac{\partial\eta}{\partial t} - \frac{\partial\phi}{\partial x}\frac{\partial\eta}{\partial x} - \frac{\partial\phi}{\partial y}\frac{\partial\eta}{\partial y}\right) + \eta\frac{\partial}{\partial z}\left(\frac{\partial\phi}{\partial z} - \frac{\partial\eta}{\partial t} - \frac{\partial\phi}{\partial x}\frac{\partial\eta}{\partial x} - \frac{\partial\phi}{\partial y}\frac{\partial\eta}{\partial y}\right) + \cdots = 0 \quad \text{on } z = 0, \tag{6}$$

$$\left(\frac{\partial\phi}{\partial t} + g\eta + \frac{1}{2}|\nabla\phi|^2\right) + \eta\frac{\partial}{\partial z}\left(\frac{\partial\phi}{\partial t} + g\eta + \frac{1}{2}|\nabla\phi|^2\right) + \cdots = 0 \quad \text{on } z = 0. \tag{7}$$

Correspondingly, we can write

$$\phi = \varepsilon\phi^{(1)} + \varepsilon^2\phi^{(2)} + \cdots, \tag{8}$$

$$\eta = \varepsilon\eta^{(1)} + \varepsilon^2\eta^{(2)} + \cdots, \tag{9}$$

where ε is a perturbation parameter which is usually related to wave slope and the superscripts 1 and 2 denote the first- and second-order components of the potential, respectively. The components are further split into $\phi^{(k)} = \phi_I^{(k)} + \phi_D^{(k)}$, where $\phi_I^{(k)}$ are the known incident potentials and $\phi_D^{(k)}$ the unknown diffracted potentials. Substituting Eqs. (8) and (9) into (1)–(5), the governing equations for $\phi_D^{(k)} (k = 1, 2)$ become.

$$\nabla^2\phi_D^{(k)} = 0 \quad \text{in } \Omega_f^{(0)}, \tag{10}$$

and the boundary conditions based on the order of ε become

$$\frac{\partial\phi_D^{(k)}}{\partial z} - \frac{\partial\eta_D^{(k)}}{\partial t} = f_k' \quad \text{on } z = 0, \tag{11}$$

$$\frac{\partial\phi_D^{(k)}}{\partial t} + g\eta_D^{(k)} = f_k'' \quad \text{on } z = 0, \tag{12}$$

$$\frac{\partial\phi_D^{(k)}}{\partial n} = -\frac{\partial\phi_I^{(k)}}{\partial n} \quad \text{on } S_b^{(0)}, \tag{13}$$

$$\frac{\partial \phi_D^{(k)}}{\partial z} = 0 \quad \text{on } z = -h, \tag{14}$$

where $\Omega_f^{(0)}$ is the fixed fluid domain below $z = 0$ and $S_b^{(0)}$ is the body surface below the mean water level. The terms f_k' and f_k'' in these equations are:

$$f_1' = 0,$$
$$f_2' = -\left(\frac{\partial \phi_I^{(2)}}{\partial z} - \frac{\partial \eta_I^{(2)}}{\partial t}\right) + \frac{\partial \phi^{(1)}}{\partial x}\frac{\partial \eta^{(1)}}{\partial x} + \frac{\partial \phi^{(1)}}{\partial y}\frac{\partial \eta^{(1)}}{\partial y} - \eta^{(1)}\frac{\partial^2 \phi^{(1)}}{\partial z^2},$$
$$f_1'' = 0,$$
$$f_2'' = -\left(\frac{\partial \phi_I^{(2)}}{\partial t} + g\eta_I^{(2)}\right) - \frac{1}{2}\left|\nabla \phi^{(1)}\right|^2 - \eta^{(1)}\frac{\partial^2 \phi^{(1)}}{\partial z \partial t},$$

where $\eta_I^{(1)}$ and $\eta_I^{(2)}$ are the first- and second-order incident wave elevations, respectively. The incident wave and potential are transient in general. For the periodic Stokes wave, they can be written as

$$\eta_I = \varepsilon \eta_I^{(1)} + \varepsilon^2 \eta_I^{(2)} = \frac{H}{2}\cos k_0(x - ct) + \left(\frac{H}{2}\right)^2 \frac{k_0}{4}\frac{\cosh k_0 h(\cosh 2k_0 h + 2)}{\sinh^3 k_0 h}\cos 2k_0(x - ct), \tag{15}$$

$$\phi_I = \varepsilon \phi_I^{(1)} + \varepsilon^2 \phi_I^{(2)} = \frac{H}{2}c\frac{\cosh k_0(z + h)}{\sinh k_0 h}\sin k_0(x - ct) + \frac{3}{8}\left(\frac{H}{2}\right)^2 k_0 c\frac{(\cosh 2k_0(z + h)}{\sinh^4 k_0 h}\sin 2k_0(x - ct), \tag{16}$$

where H is the wave height, c the wave celerity and k_0 the wavenumber. The wave frequency can be written as $\omega = k_0 c$ and is linked to the wavenumber through $k_0 \tanh k_0 h = \omega^2/g$.

The hydrodynamic forces on the cylinder can be calculated by integration of the pressure over its wetted surface S_b. For second order problems, the equation can be written as [e.g., Issacson and Cheung (1992)]

$$F_j = -\rho \iint_{s_b^{(0)}} \left(\frac{\partial \phi^{(1)}}{\partial t} + \frac{\partial \phi^{(2)}}{\partial t} + \frac{1}{2}\nabla \phi^{(1)} \nabla \phi^{(1)} + gz\right) n_j \, \mathrm{d}s + \frac{1}{2}\rho g \int_l (\eta^{(1)})^2 n_j \mathrm{d}l \quad (j = 1, 2, \cdots, 6), \tag{17}$$

where ρ is the density of the fluid, $(n_1, n_2, n_3, n_4, n_5, n_6) = (n_x, n_y, n_z, yn_z - zn_y, zn_x - xn_z, xn_y - yn_x)$, and $j = 1,2,3$ corresponding to the force (F_x, F_y, F_z) and $j = 4,5,6$ to the moment (M_x, M_y, M_z). The last term in Eq. (17) is due to the variation of S_b with water surface and l is the mean waterline. The force can be further split into three components,

$$F_j = F_j^{(1)} + F_j^{(2)} + \bar{F}_j^{(2)}, \tag{18}$$

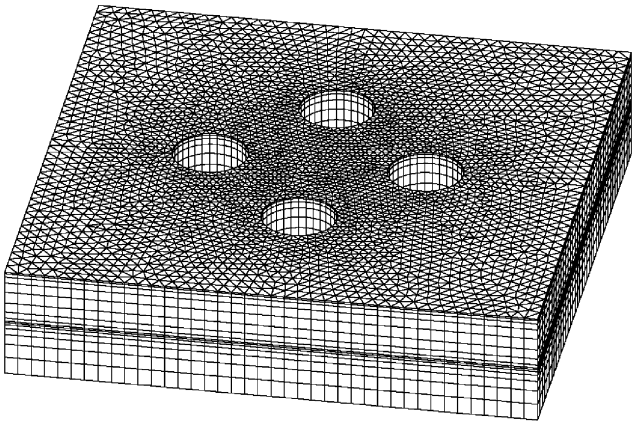

Fig. 2. A 3-D mesh for four truncated cylinders.

where

$$F_j^{(1)} = -\rho \iint_{S_b^{(0)}} \frac{\partial \phi^{(1)}}{\partial t} n_j \, \mathrm{d}s \quad (j = 1, 2, \cdots, 6) \tag{19}$$

is the first-order oscillatory force, and

$$F_j^{(2)} = F_j^{(21)} + F_j^{(22)} - \bar{F}_j^{(2)} \quad (j = 1, 2, \cdots 6), \tag{20}$$

is the second-order oscillatory force. The components in Eq. (20) are defined as

$$F_j^{(21)} = -\frac{1}{2}\rho \iint_{S_b^{(0)}} \left|\nabla \phi^{(1)}\right|^2 n_j \, \mathrm{d}s + \frac{1}{2}\rho g \int_l (\eta^{(1)})^2 n_j \, \mathrm{d}l \ \ (j = 1, 2, \cdots, 6), \tag{21}$$

$$F_j^{(22)} = -\rho \iint_{S_b^{(0)}} \frac{\partial \phi^{(2)}}{\partial t} n_j \quad \mathrm{d}s \ \ (j = 1, 2, \cdots, 6), \tag{22}$$

$$\bar{F}_j^{(2)} = -\frac{1}{2}\rho \overline{\iint_{S_b^{(0)}} \left|\nabla \phi^{(1)}\right|^2 n_j \, \mathrm{d}s} + \frac{1}{2}\rho g \overline{\int_l (\eta^{(1)})^2 n_j \, \mathrm{d}l} \ \ (j = 1, 2, \cdots, 6). \tag{23}$$

Evidently, $F_j^{(21)}$ is due to only the first-order potential and wave elevation and $F_j^{(22)}$ is due to the second-order potential. $\bar{F}_j^{(2)}$ is the steady mean drift force and the overbar means the average over time. Its presence is due to the fact that the mean of the product of periodic functions may not be zero.

3. Finite element discretisation and numerical procedure

We use the finite element method here. A 2-D mesh generator called BAMG (Hecht, 1998) is used to generate the unstructured 2-D grid on the plane first. It is then extended along the vertical direction to form the 3-D mesh with prismatic elements, as shown in Fig. 2 for four truncated cylinders. The procedure is similar to that in the work by Wu and Hu (2004), where the 2-D mesh is based on a tri-tree algorithm.

The disturbances due to water waves usually decay very rapidly along the depth. It will therefore be more rational to use smaller elements near the free surface and larger elements near the bottom. One way to achieve this to use the

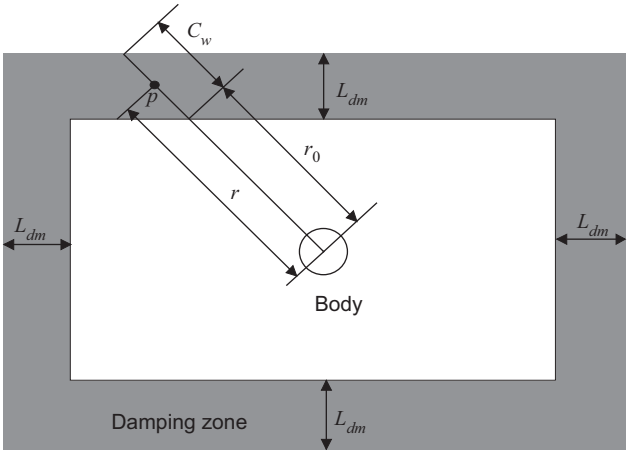

Fig. 3. Damping zone on the free surface.

following equation along the depth (Chung, 2002):

$$z_i = -h\frac{(\beta+1)-(\beta-1)(\beta+1/\beta-1)^{1-i/m}}{(\beta+1/\beta-1)^{1-i/m}+1} \quad (i=0,1,\cdots,m), \tag{24}$$

where z_i is the vertical coordinate of the element node at layer i and m is the number of layers; $\beta>1$ in the equation is a constant. A smaller β will lead the elements to cluster near the free surface and a larger β will have the elements distribute more uniformly along the depth. This equation can also be modified to have elements cluster at both ends, which can be useful for a truncated cylinder because of its sharp edge near the bottom.

Once the mesh is generated, the potentials $\phi^{(k)}(k=1,2)$ can be expressed in terms of the shape function $N_J(x,y,z)$,

$$\phi^{(k)} = \sum_{J=1}^{n} \phi_J^{(k)} N_J(x,y,z), \tag{25}$$

where $\phi_J^{(k)}$ are the potentials at node J and n is the number of nodes. Based on the Galerkin method, we have

$$\iiint_{\Omega_f^{(0)}} \nabla^2\phi^{(k)} N_i \mathrm{d}\Omega = 0. \tag{26}$$

Using Green's identity and the boundary conditions, we can obtain the following matrix equation:

$$[K]\{\phi^{(k)}\} = \{F^{(k)}\} \quad (k=1,2), \tag{27}$$

where

$$K_{IJ} = \iiint_{\Omega_f^{(0)}} \nabla N_I \nabla N_J \mathrm{d}\Omega \ (I\notin S_p \ \& \ J\notin S_p), \quad F_I^{(k)} = \iint_{S_n} N_I f_n^{(k)} \mathrm{d}S - \iiint_{\Omega_f^{(0)}} \nabla N_I \sum_{\substack{J=1 \\ (J\in S_p)}}^{n} (f_p^{(k)})_J \nabla N_J \mathrm{d}\Omega \ (I\notin S_p).$$

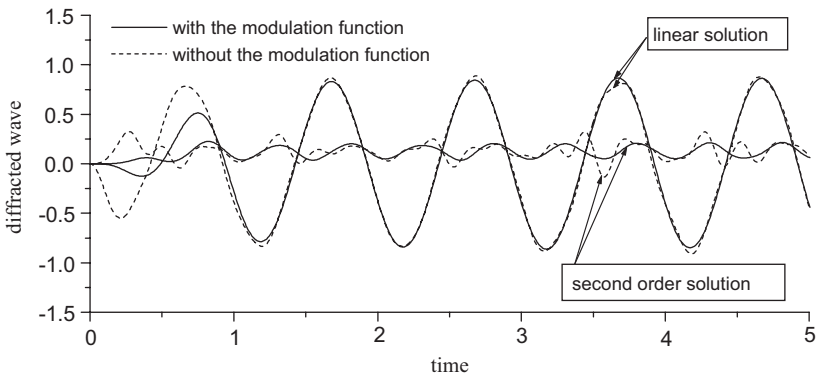

Fig. 4. Comparison of waves with and without modulation function.

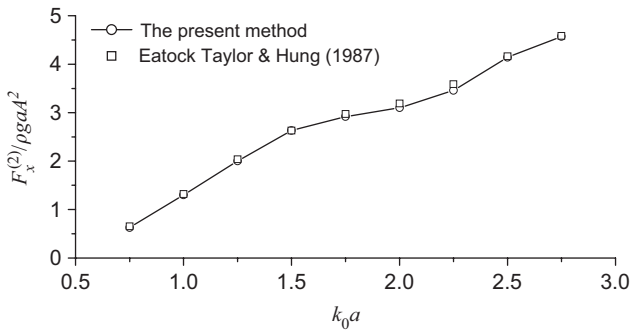

Fig. 5. The amplitude of the total second order force versus k_0a.

S_p in the above equations represents the Dirichlet boundary on which the potentials, denoted by $f_p^{(k)}(k=1,2)$, are known, and S_n represents the Neumann boundary on which the normal derivatives of the potentials, denoted by $f_n^{(k)}(k=1,2)$, are known. The matrix equations are then solved through an iteration based on the conjugate gradient method with a symmetric successive over-relaxation (SSOR) preconditioner.

After the potential is found, its first- and second-order derivatives on element nodes are required to update $\eta_D^{(k)}$ and $\phi_D^{(k)}$ through Eqs. (11) and (12). The derivatives in theory can be obtained through the differentiation of the shape function. The accuracy is, however, usually not sufficient when the order of the shape function is low and the result becomes zero when the order of the derivative is higher than that of the shape function. Here we employ a cubic polynomial to express the velocity potential along straight mesh line in the vertical direction,

$$\phi = a + bz + cz^2 + dz^3, \tag{28}$$

where a,b,c and d can be obtained from the values ϕ at four successive nodes. The first- and second-order derivatives with respect to z can then be obtained from direct differentiation. The procedure is similar to that used by Ma et al. (2001a, b). Furthermore, their scheme for the derivatives of the potential and the wave elevation in the horizontal direction is also adopted here.

Unlike Eqs. (11) and (12), the derivatives required in Eqs. (21) and (23) may be obtained directly through differentiation of the shape function. This is because they are evaluated inside the surface element, where the accuracy through direct differentiation is usually better than that on the node. Also for the force, it is the integration of the

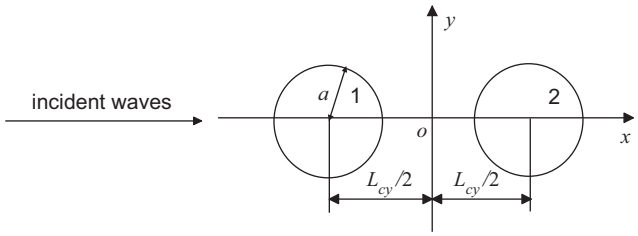

Fig. 6. Two-cylinder case.

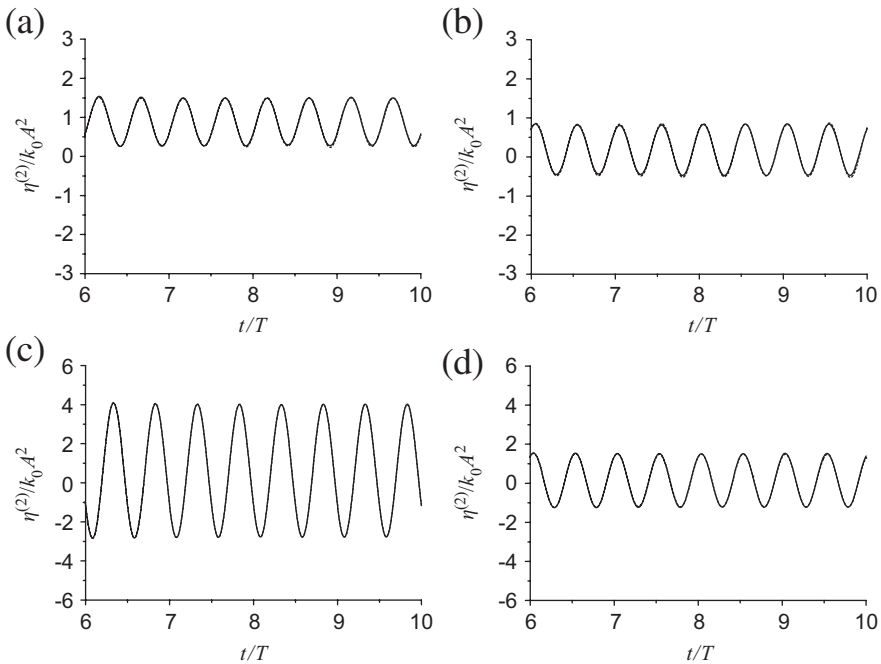

Fig. 7. Convergence of second-order waves with mesh variation in vertical direction: (a) front side of cylinder 1; (b) back side of cylinder 1; (c) front side of cylinder 2; (d) back side of cylinder 2. Dash line: $NH = 10$; Dash dot line: $NH = 14$; Solid line: $NH = 18$.

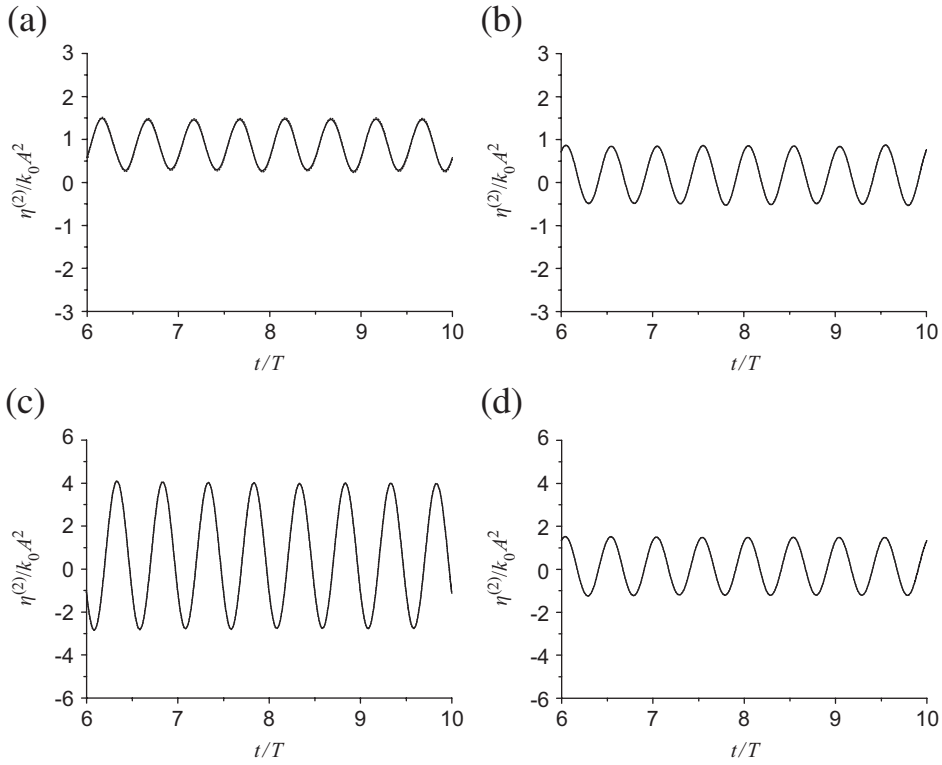

Fig. 8. Convergence of second-order waves with mesh variation in horizontal direction: (a) front side of cylinder 1; (b) back side of cylinder 1; (c) front side of cylinder 2; (d) back side of cylinder 2. Solid line: mesh with 15024 nodes and 29658 elements; Dash line: mesh with 8706 nodes and 17122 elements.

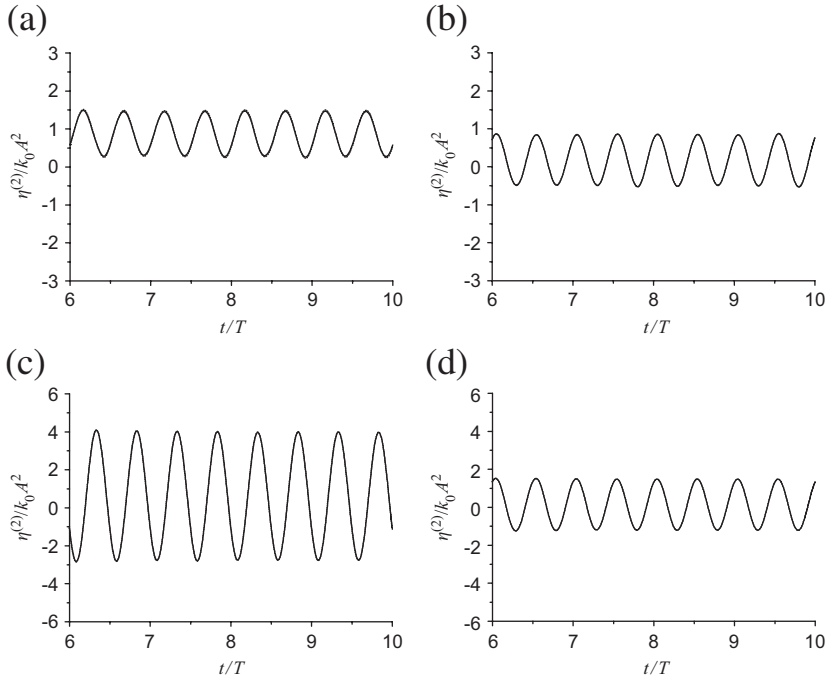

Fig. 9. Convergence of second-order waves with time interval variation: (a) front side of cylinder 1; (b) back side of cylinder 1; (c) front side of cylinder 2; (d) back side of cylinder 2. Dash line: $\Delta t = T/200$; Solid line: $\Delta t = T/400$.

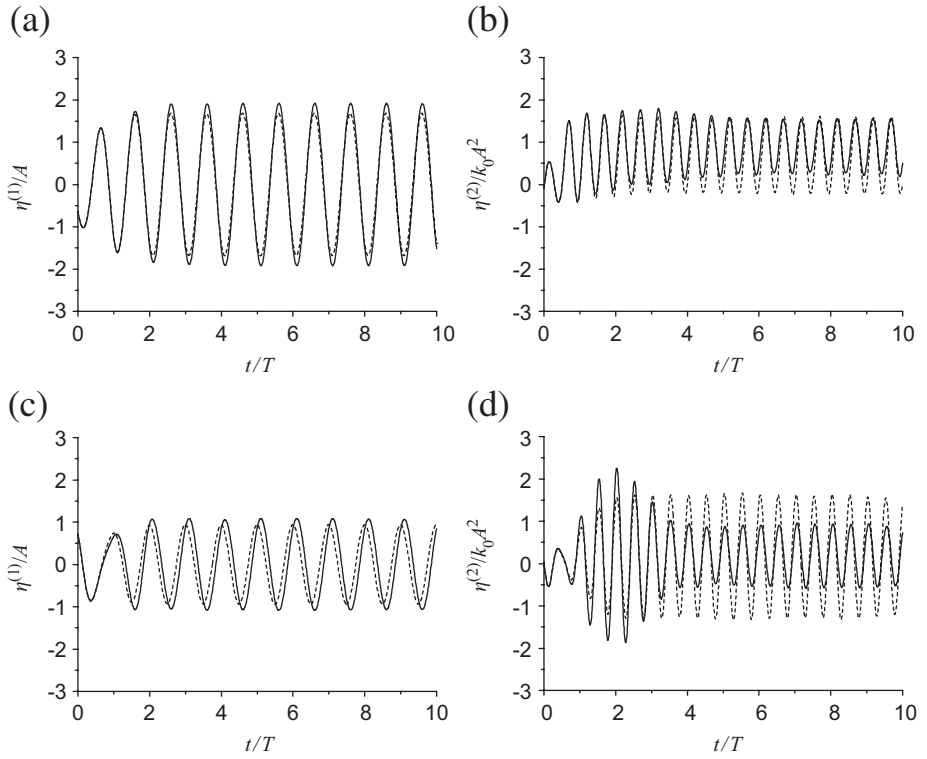

Fig. 10. Wave run-up along cylinder 1: (a) first-order, front side; (b) second-order, front side; (c) first-order, back side; (d) second-order, back side. Dash line: single-cylinder; Solid line: two-cylinder.

function rather than the function itself which is needed. The result is therefore less sensitive to the accuracy at an individual point. Thus the derivatives can be obtained from

$$\begin{bmatrix} \frac{\partial\phi}{\partial x} \\ \frac{\partial\phi}{\partial y} \\ \frac{\partial\phi}{\partial z} \end{bmatrix} = \begin{bmatrix} \frac{\partial x}{\partial\xi} & \frac{\partial y}{\partial\xi} & \frac{\partial z}{\partial\xi} \\ \frac{\partial x}{\partial\eta} & \frac{\partial y}{\partial\eta} & \frac{\partial z}{\partial\eta} \\ n_x & n_y & n_z \end{bmatrix}^{-1} \begin{bmatrix} \frac{\partial\phi}{\partial\xi} \\ \frac{\partial\phi}{\partial\eta} \\ \frac{\partial\phi}{\partial n} \end{bmatrix}, \tag{29}$$

in which the normal derivative $\partial\phi/\partial n$ is known from the boundary condition. It is assumed in this equation that the surface element corresponds to $\zeta =$ constant, and the global coordinates (x,y,z) vary only with (ξ,η) in the local system.

The fourth-order Adams–Bashforth scheme is used to advance the simulation through time stepping method. This scheme provides a high-order accuracy and is particularly suited for the solution based on the perturbation procedure. As the mesh is fixed and no remeshing is applied throughout the simulation, the information at previous time steps can be stored easily. For the fully nonlinear problem where the domain changes and remeshing is applied, this scheme could be problematic, as the information on the new nodes at previous steps needs to be obtained through interpolation. Thus, Wang and Wu (2006) adopted the fourth-order Runge–Kutta method in their fully nonlinear simulation for a 2-D flared body. Mini steps were required for each time step Δt. Because no remeshing was applied within Δt, no interpolation was required. The scheme provides an accuracy similar to the fourth order Adams–Bashforth method, but it requires more CPU because of the extra computational effort for the mini steps.

For long time simulations, an appropriate radiation condition should be imposed on the boundary S_c to minimize the wave reflection. Here we use a combination of Sommerfeld–Orlanski condition and a damping zone. The Sommerfeld–Orlanski condition used is based on that in Issacson and Cheung (1992). The damping zone adopted is

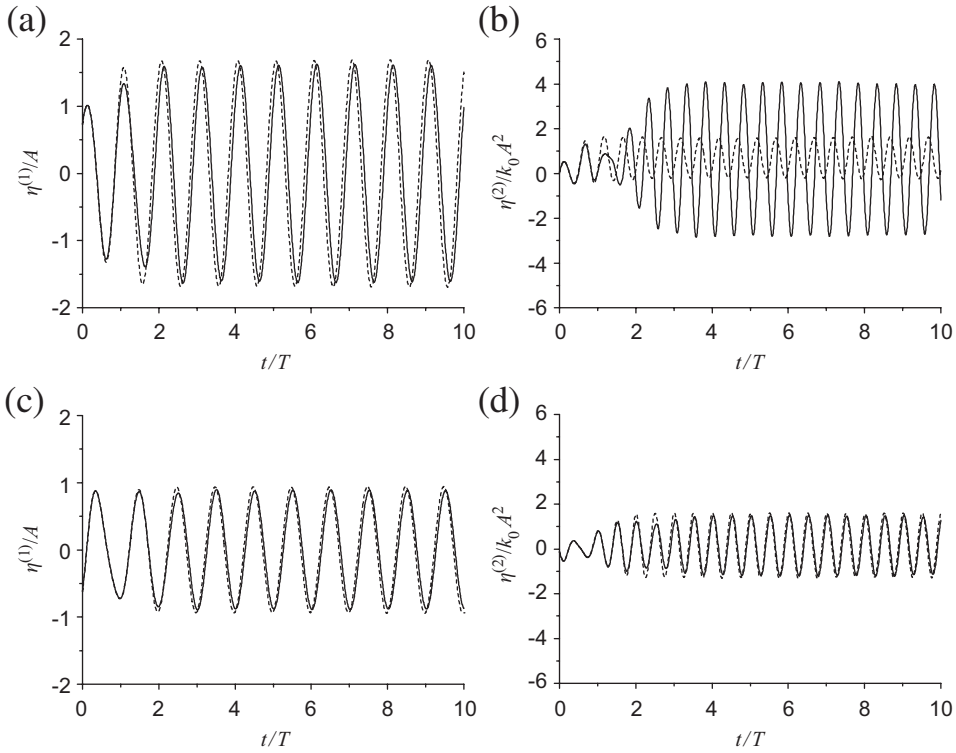

Fig. 11. Wave run-up along cylinder 2: (a) first-order, front side; (b) second-order, front side; (c) first-order, back side; (d) second-order, back side. Dash line: single-cylinder; Solid line: two-cylinder.

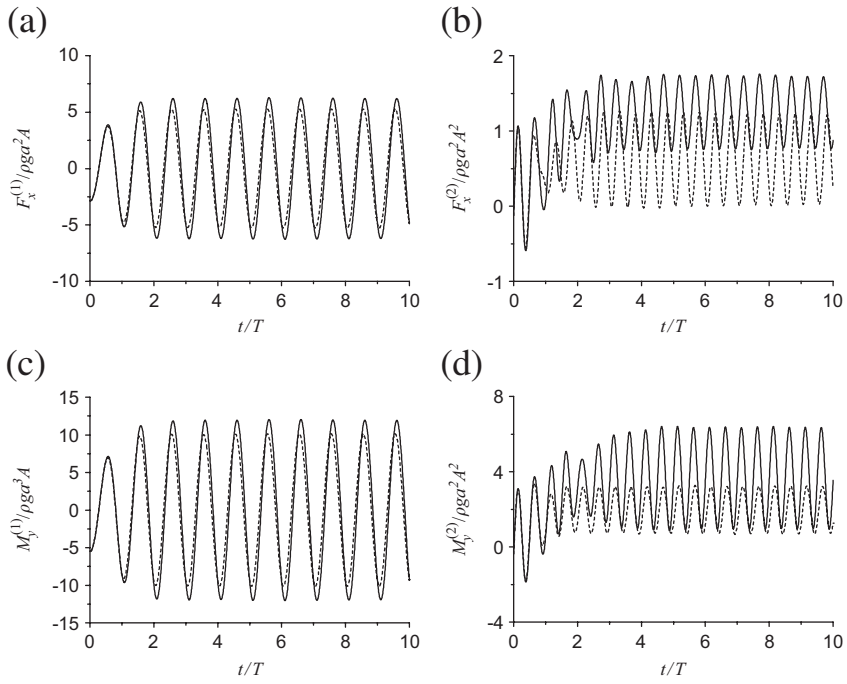

Fig. 12. Force and moment on cylinder 1. Dash line: single-cylinder; Solid line: two-cylinder.

similar to that used by Nakos et al. (1993) for the linear problem. We rewrite Eq. (11) as

$$\frac{\partial \eta_D^{(k)}}{\partial t} = \frac{\partial \phi_D^{(k)}}{\partial z} - f'_k - 2\nu\eta_D^{(k)} + \frac{\nu^2}{g}\phi_D^{(k)} \ (k = 1, 2) \ \text{on} \ z = 0, \tag{30}$$

where ν is the damping coefficient given by

$$\nu(r) = 3\frac{C_s}{C_w^3}(r - r_0)^2 \quad 0 \leqslant r - r_0 \leqslant C_w. \tag{31}$$

In Eq. (31) r is the distance for the point under consideration to the centre of the nearest cylinder. For the single body shown in Fig. 3, the damping zone starts from the edge of an inner rectangle $r = r_0(x,y)$ and ends at the outer rectangle $r = r_0(x,y) + C_w(x,y)$. C_s in the equation is a constant to control the strength of the damping coefficient and is chosen to be 1.0 in this study, and the width of the damping zone L_{dm} (see Fig. 3) is set to be one wavelength for short waves and eight times the radius of the cylinder for long waves.

4. Numerical results

The cases considered below correspond to the situations where cylinders are suddenly placed in periodic waves. In the numerical simulation, however, the body surface boundary condition is not imposed immediately but satisfied gradually. A modulation function $M(t)$ is applied in Eq. (13) in a manner similar to that in Isaacson and Cheung (1992), or

$$\frac{\partial \phi_D^{(k)}}{\partial n} = -M(t)\frac{\partial \phi_I^{(k)}}{\partial n} \quad (k = 1, 2), \tag{32}$$

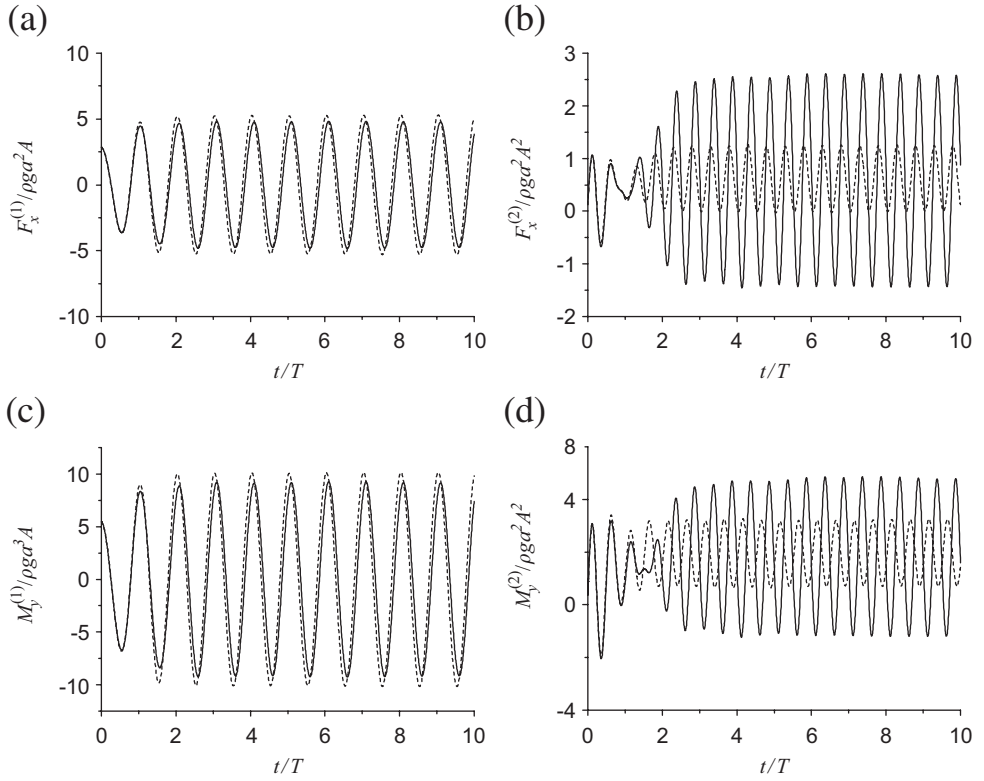

Fig. 13. Force and moment on cylinder 2. Dash line: single-cylinder; Solid line: two-cylinder.

where

$$M(t) = \begin{cases} \frac{1}{2}\left[1 - \cos\left(\frac{\pi t}{T}\right)\right] & t < T, \\ 1, & t \geqslant T, \end{cases}$$

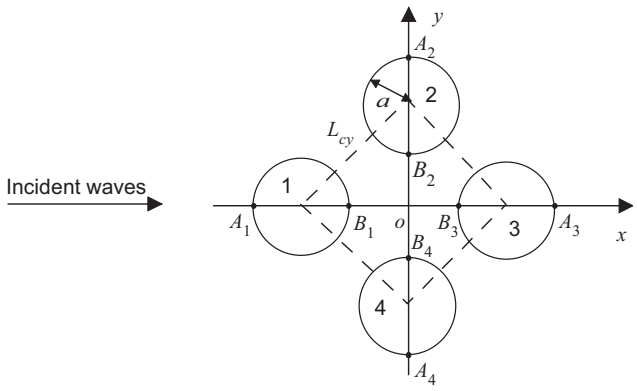

Fig. 14. Four-cylinder case.

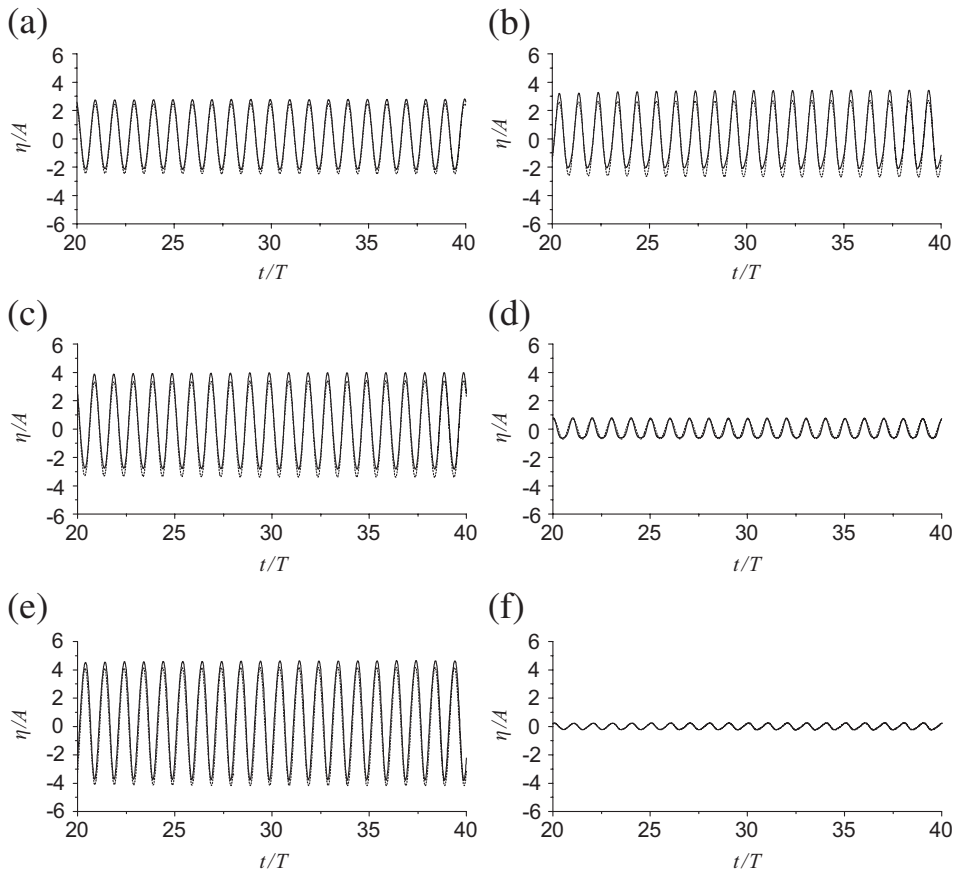

Fig. 15. Run-ups along cylinders at $k_0 a = 1.66$: (a) A_1; (b) B_1; (c) B_2 and B_4; (d) A_2 and A_4; (e) B_3; (f) A_3. Dash line: linear; Solid line: linear plus second order.

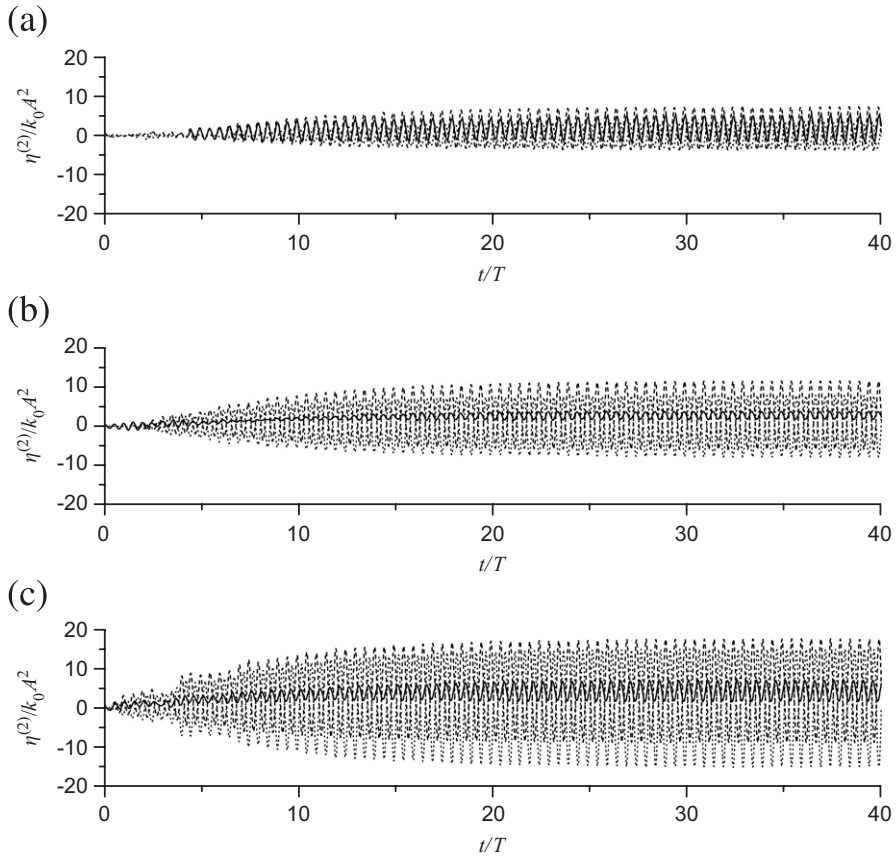

Fig. 16. Second-order wave histories at $k_0a = 1.66$: (a) B_1; (b) B_2 & B_4; (c) B_3. Dash line: $\eta^{(21)}$; Dot line: $\eta^{(22)}$; Solid line: $\eta^{(2)}$.

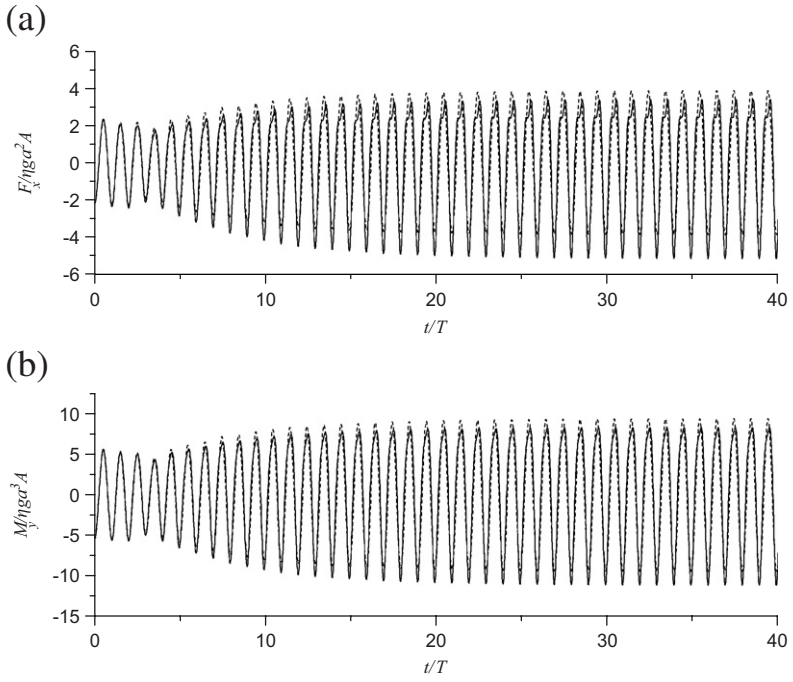

Fig. 17. Histories of force and moment on cylinder 3 at $k_0a = 1.66$. Dash line: linear; Solid line: linear plus second order.

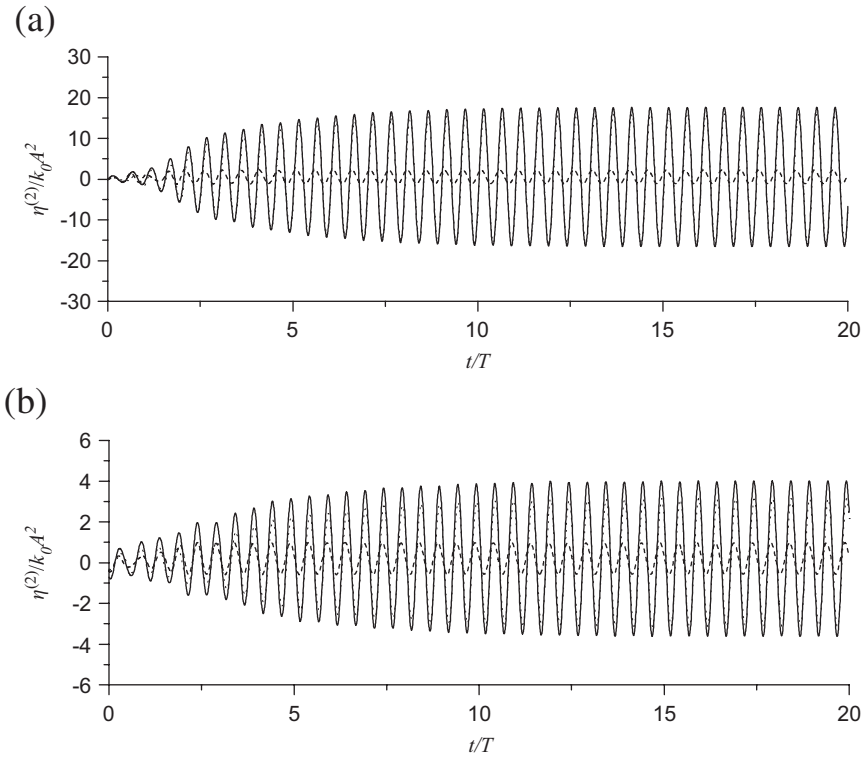

Fig. 18. Second-order wave histories for cylinder 3 at $k_0a = 0.468$: (a) B_3; (b) A_3. Dash line: $\eta^{(21)}$; Dot line: $\eta^{(22)}$; Solid line: $\eta^{(2)}$.

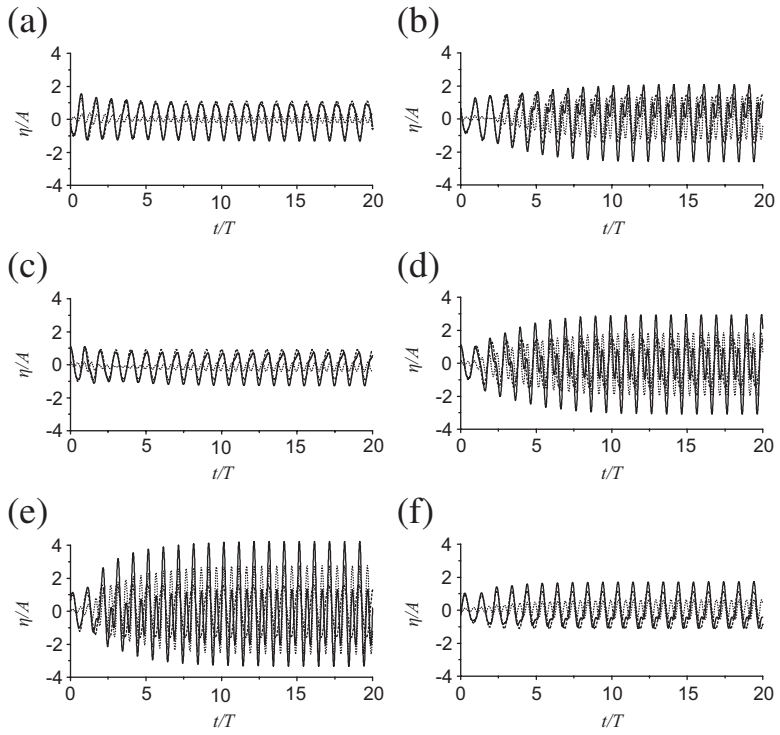

Fig. 19. Wave histories for cylinders 1, 2 and 3 at $k_0a = 0.468$: (a) A_1; (b) B_1; (c) A_2; (d) B_2; (e) B_3; (f) A_3. Dash line: linear; Solid line: linear plus second order.

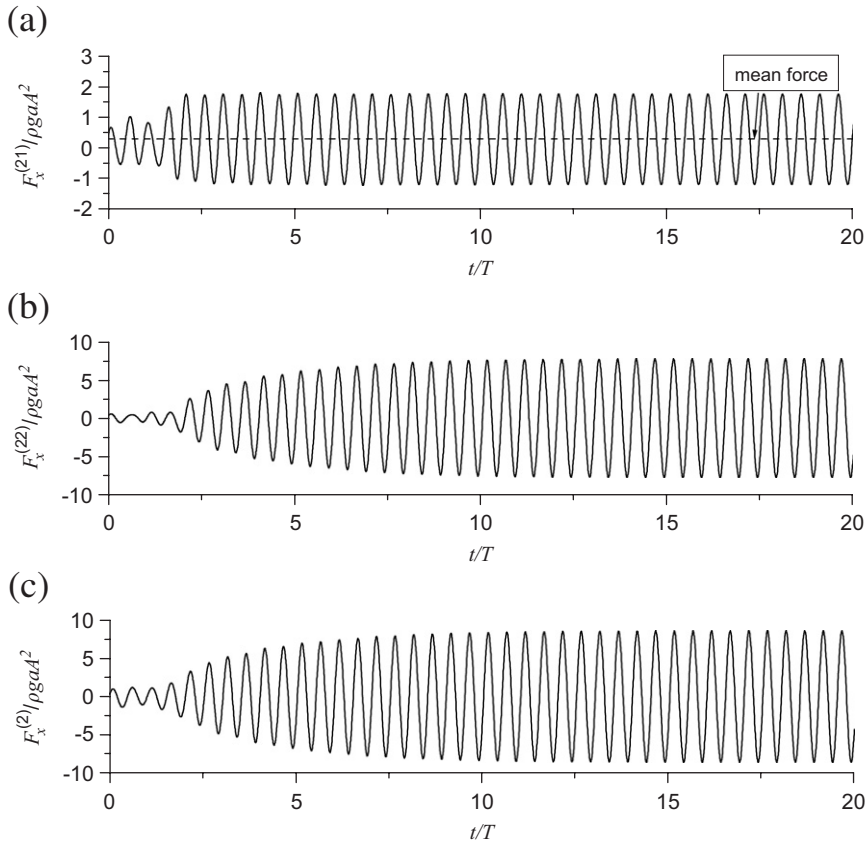

Fig. 20. Histories of second-order forces on cylinder 3 at $k_0 a = 0.468$.

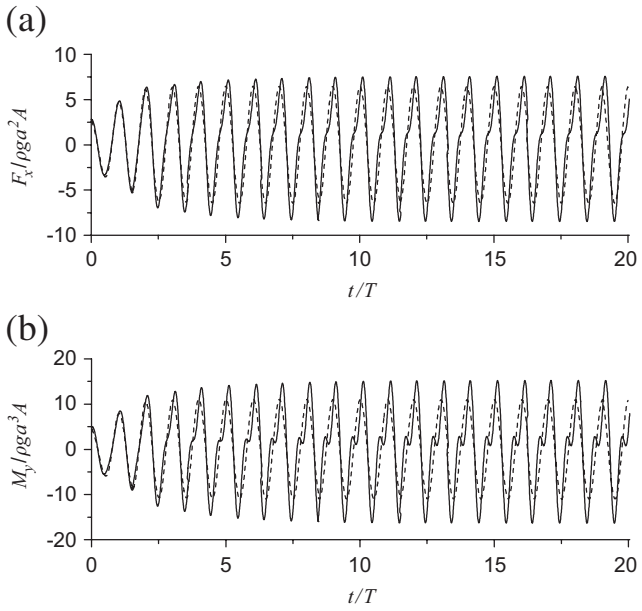

Fig. 21. Histories of force and moment on cylinder 3 at $k_0 a = 0.468$. Dash line: linear; Solid line: linear plus second order.

and $T = 2\pi/\omega$ is the wave period. The use of the modulation function helps the diffracted wave to reach the periodic state more smoothly and quickly. A comparison between results with and without the modulation function is shown in Fig. 4. It is clearly seen that the first-order wave without the modulation function has some noise and the second-order wave has no sign of reaching the periodic state even after five periods. The adoption of the modulation function has greatly improved the result.

In all the simulations below, the cylinders are identical and all have radius a. The water depth is taken as $3a$. The ratio of the wave height to wavelength is taken as $H/L = 0.05$ and $A = H/2$.

Before considering the cases of multi-cylinders, we first undertake a simulation for a single cylinder with its centre located at (0, 0). The amplitude of the second order force versus k_0a is given in Fig. 5, in which the result from Eatock Taylor and Hung (1987) is also given as comparison. It is seen that the agreement is very good.

4.1. Two cylinders

A further simulation for a two-cylinder case is considered. The two cylinder configuration is the simplest multi-cylinder case. Fig. 6 shows that two bodies are placed along the line of the wave direction. The centres of the two cylinders are located at $(-L_{cy}/2,0)$ and $(L_{cy}/2,0)$. The simulation corresponds to $L_{cy} = 4a$ and $k_0a = 0.754$.

A convergence study is first undertaken. In this case, the fluid domain on the free surface is of rectangular shape with length $50a$ and width $40a$, which are divided into 60 and 50 intervals, respectively. This corresponds to a mesh with 8706 nodes and 17 122 elements on the free surface. The waterline of one cylinder is divided into 36 uniform segments and the time step is taken as $\Delta t = T/200$. Three different vertical meshes with $NH = 10$, 14 and 18 are used and the corresponding results for second-order waves are shown in Fig. 7. The three curves are in good agreement and the results at $NH = 14$ and 18 are almost graphically identical. The simulation is made on a Pentium 4 personal computer with 3.40 GHz Intel CPU, windows XP system and Open Watcom C++ complier v1.1. The maximum memory is about 74 MB at $NH = 14$ and 93 MB at $NH = 18$. The CPU required is about 10 s per time step at $NH = 14$ and 14 s at $NH = 18$, respectively. It ought to be pointed out that the solution is obtained using an iterative method. For very long simulations, an alternative would be to use triangular decomposition of the banded matrix. The decomposition may take some CPU, but once it has been done it can be used over all the time steps and therefore the subsequent CPU is relatively negligible. However, it is also important to notice that the decomposition method may take much more

Table 1
Second-order wave amplitudes at points B_1 and B_3

Location	$\lvert\eta^{(21)}\rvert/k_0A^2$		$\lvert\eta^{(22)}\rvert/k_0A^2$		$\lvert\eta^{(2)}\rvert/k_0A^2$	
	Present method	Frequency-domain	Present method	Frequency-domain	Present method	Frequency-domain
B_1	1.41	1.44	8.87	9.12	7.93	8.05
B_3	1.74	1.72	15.96	16.68	17.10	17.72

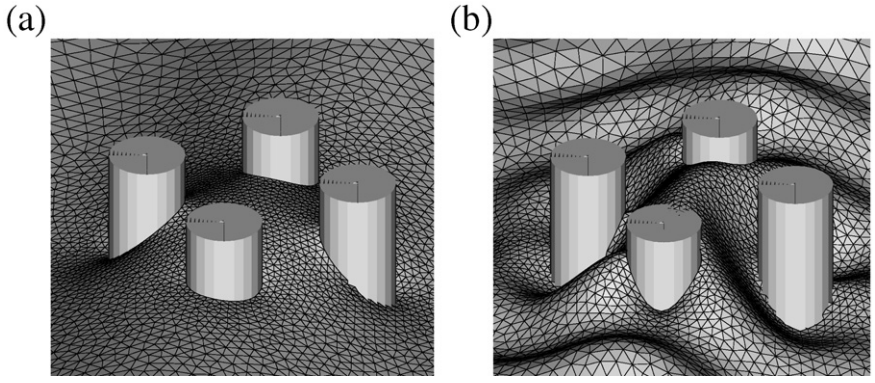

Fig. 22. Wave profiles at $t = 16\,T$ and $k_0a = 0.468$: (a) linear; (b) linear plus second order.

memory because the zeros within the band cannot be squeezed out as in the iterative method. This is part of the reasons that the iterative method is used here when simulations are made over several thousand steps.

A convergence study is further undertaken with horizontal elements. The numbers of nodes and elements on the free surface used above have been increased to 15 024 nodes and 29 658 elements, respectively. The simulation is performed with $NH = 14$ and $\Delta t = T/200$. The results are shown in Fig. 8, and the agreement from the two meshes is quite good. Convergence study is also undertaken with the time steps using $\Delta t = T/200$ and $= T/400$ at $NH = 14$. The result is shown in Fig. 9 and the agreement is again quite good.

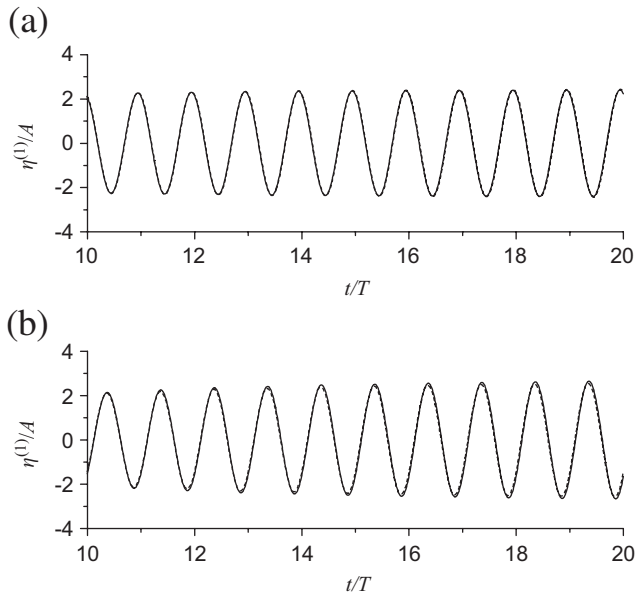

Fig. 23. First-order wave histories for cylinder 1 at $k_0a = 1.66$: (a) front; (b) back. Dash line: bottom mounted; Solid line: truncated.

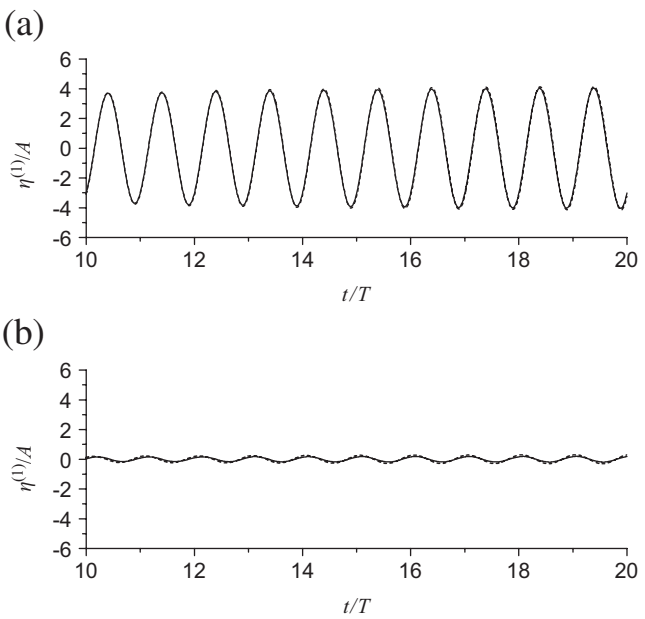

Fig. 24. First-order wave histories for cylinder 3 at $k_0a = 1.66$: (a) front; (b) back. Dash line: bottom mounted; Solid line: truncated.

Further comparisons between single- and two-cylinder cases at $NH = 14$ and $\Delta t = T/200$ are made and results are included in Figs. 10 and 11. The single cylinder is placed at the location of cylinder 1 in Fig. 10 and at the location of cylinder 2 in Fig. 11. As the body surface boundary condition is modulated through $M(t)$, the wave run-up becomes periodic after one wave period for the single cylinder case, as in Issacson and Cheung (1992). The transition to periodic sate, however, takes much longer in the two cylinder case, especially for the second-order results, as can be seen from the figures. The interaction effect on the first-order run-up is evidently visible, but the major effect is on the second order. In fact, it is observed that the amplitude of $\eta^{(2)}$ at the front side of cylinder two is about 3.7 times that of a single

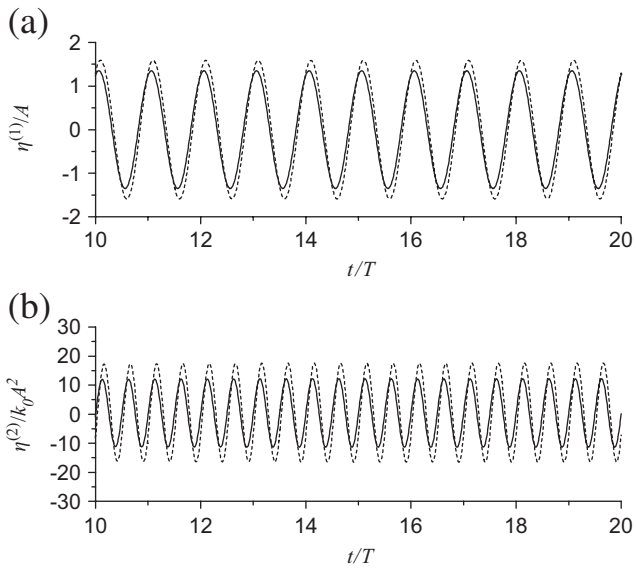

Fig. 25. Wave histories at the front side of cylinder 3 at $k_0a = 0.468$: (a) linear; (b) second order. Dash line: bottom mounted; Solid line: truncated.

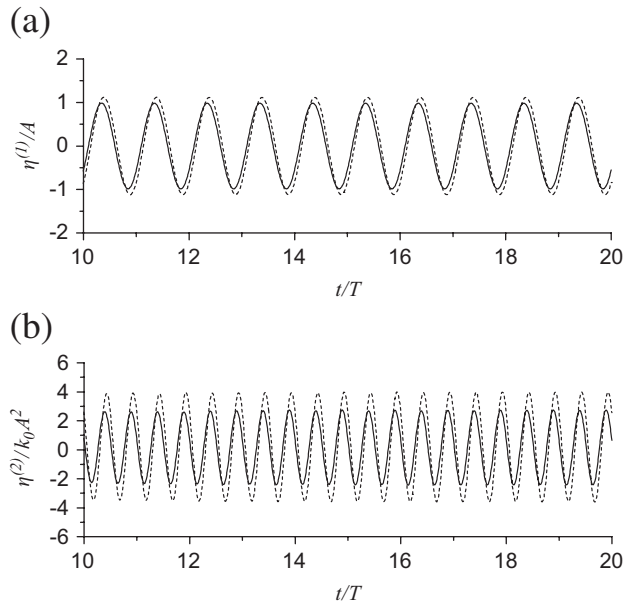

Fig. 26. Wave histories at the back side of cylinder 3 at $k_0a = 0.468$; (a) linear; (b) second order. Dash line: bottom mounted; Solid line: truncated.

cylinder. Figs. 12 and 13 give the force and moment on the two cylinders. Similar to the wave run-up, the results for two cylinder case take a longer time to become periodic, especially for the second-order force and moment. The interaction between two cylinders leads to much bigger second-order results, both in terms of the magnitude and the mean value.

4.2. Four cylinders

A four cylinder case with $L_{cy} = 4a$ is considered in this section. The configuration shown in Fig. 14 is symmetric about x and y-axes. This is the case considered by Evans and Porter (1997b) based on the linear theory and by Malenica et al. (1999) based on the second-order theory in the frequency domain. When $k_0a = 1.66$, it is very close to the trapped mode. The trapped mode is a localized phenomenon with finite energy which does not propagate into infinity (Ursell, 1951). Simulation is made and the wave history for the four cylinders is shown in Fig. 15, with the locations of points A_i,B_i ($i = 1,2,3,4$) given in Fig. 14. It can be seen that the maximum ratio of η/A is around 4 which is much larger than 1.85 for the single cylinder case. It ought to be pointed out that the maximum ratio will increase dramatically when L_{cy}/a is reduced, as observed in the frequency domain analysis (Evans and Porter, 1997b). We do not undertake extensive simulation for the cases with small gap between cylinders, as its practical interest is limited.

When the first-order result is large, one would expect that the second-order result would be even larger because of those product terms in Eq. (12) when $k = 2$. We give the second-order waves in Fig. 16 together with their components $\eta^{(21)}$ due to the product terms of the first-order result and $\eta^{(22)} = -(1/g)(\partial\phi^{(2)}/\partial t)$ due to the second-order potential. It is seen that the wave run-ups at $B_i(i = 2,3,4)$ have large components $\eta^{(21)}$ and $\eta^{(22)}$. The magnitudes of $\eta^{(21)}$ and $\eta^{(22)}$ are close but their phases are almost opposite to each other. Thus $\eta^{(2)}$ itself is not particularly big at these

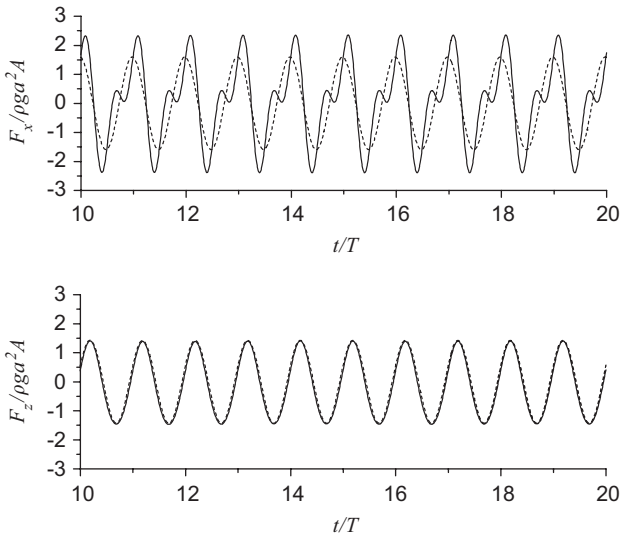

Fig. 27. Histories of forces on cylinder 3 at $k_0a = 0.468$. Dash line: linear; Solid line: linear plus second order.

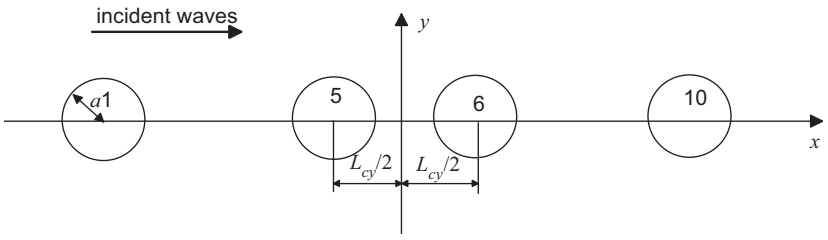

Fig. 28. Ten-cylinder case.

points. The situation at B_1 is somewhat different. There is a bigger difference between the magnitudes of $\eta^{(21)}$ and $\eta^{(22)}$, even though their phases are almost opposite to each other, and as a result $\eta^{(2)}$ is much bigger. Thus, whether the big first-order result will lead to a big second-order result depends also on the behaviour of each individual component.

The corresponding hydrodynamic force and moment on cylinder three at $k_0a = 1.66$ are shown in Fig. 17. Generally, the dominant part of the total result at this frequency and this wave height is the linear one. However, the second-order effect is also quite noticeable in this case. It is interesting to see that the transition of the force to the periodic state progresses rather slowly. This behaviour has some similarity to wave sloshing near the resonance (Wu et al., 1998), where the transition of the amplitude envelope is dominated by the difference between the natural frequency and the excitation frequency. When the difference is small, the development of the envelope can be very slow. It should also be pointed out, however, that the result does reach a periodic state after many periods in the present simulation as can be seen in the figure, while the oscillation of the envelope in the sloshing case will continuously depend on the difference between the natural frequency and excitation frequency.

We then consider a case with $k_0a = 0.468$ for the same configuration. The trapped mode is far away from this wavenumber and its effect on the first-order result is not expected to have any significance. At this wavenumber,

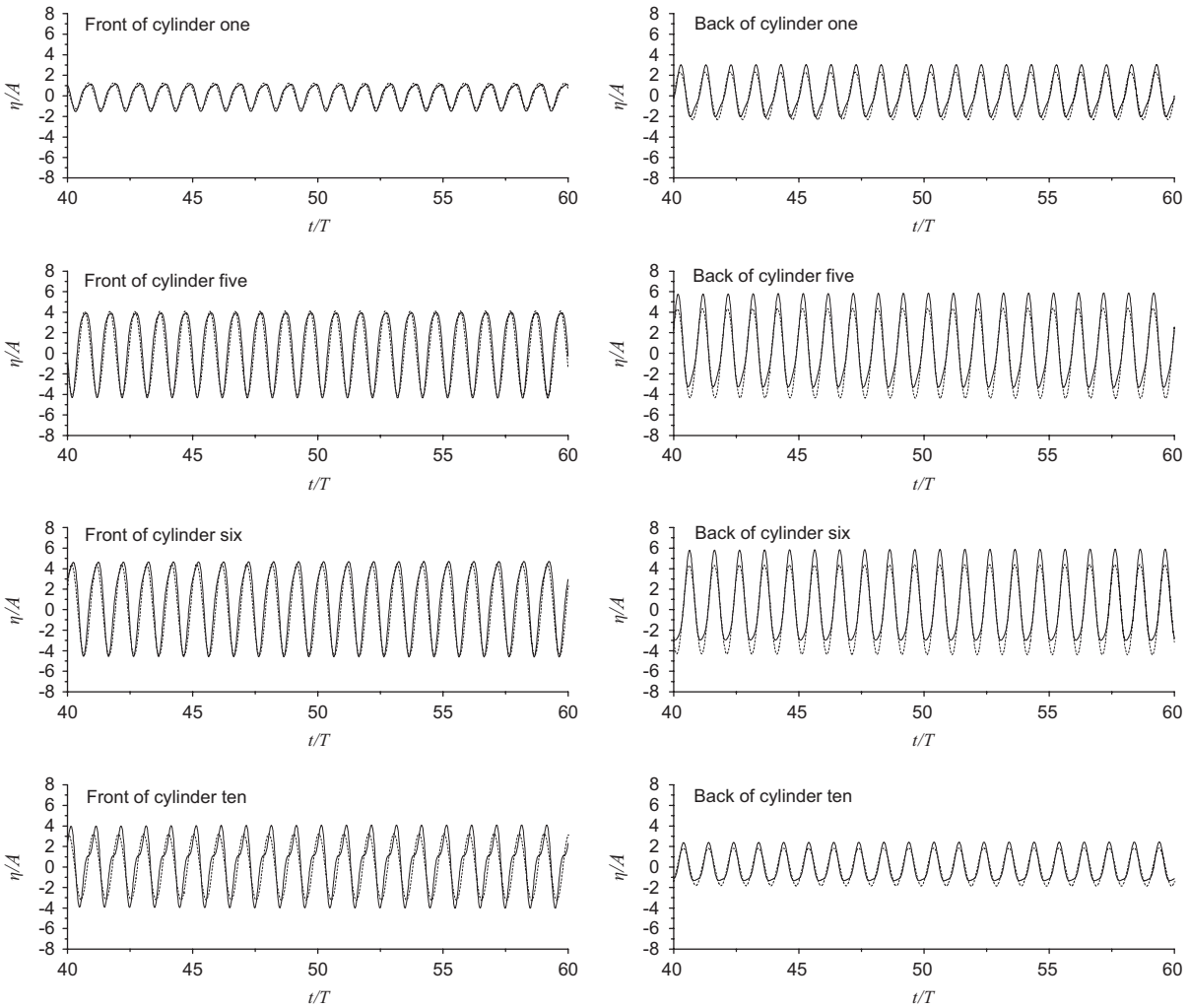

Fig. 29. Wave histories for cylinders 1, 5, 6 and 10. Dash line: linear; Solid line: linear plus second order.

however, the second-order wave corresponds to a wavenumber which is very close to the trapped mode. For this reason, the case was chosen by Malenica et al. (1999) in their second-order analysis based on the frequency domain method. As expected, all the second-order waves at A_i and B_i ($i = 1,2,3,4$) have a large component $\eta^{(22)}$ due to the second-order potential whose wavenumber is near the trapped mode. In contrast, $\eta^{(21)}$ is very small because the trapped mode virtually has no effect on the first-order result. Fig. 18 gives the second-order waves for cylinder 3. The magnitudes of the second waves at B_1, B_2 and B_3 which are in the interior region of the four cylinders are much larger than those at the exterior (A_1, A_2 and A_3). A comparison of second-order wave amplitudes at points B_1, B_3 is given in Table 1. The frequency domain results were taken from the figure by Malenica et al. (1999). The results are generally in a good agreement.

The linear and linear plus second-order waves are given in Fig. 19. It is interesting to see from Figs. 19(d) and (e) that $\eta^{(2)}$ is even larger than the first-order wave. In contrast, the amplitude of second-order wave at the front of the single cylinder is only about 20% that of the first-order at $k_0a = 0.468$ and $H/L = 0.05$. The results here of course may raise the question of whether the perturbation method is valid in this case, but it nevertheless shows some interesting behaviour near the trapped mode. It is also important to notice that if the third, fourth or higher-order potentials were included, they would not automatically be bigger than the second-order result, as their frequencies are not near that of the trapped mode. Thus if the ratio of H/L is chosen to be sufficiently small, the perturbation series is still expected to converge.

We only give the results for the force and the moment on cylinder 3 at $k_0a = 0.468$ since they are more interesting than those on other cylinders. The second-order force and moment are shown in Fig. 20 together with the components $F^{(21)}$ due to the product of the first-order result and $F^{(22)}$ due to the second-order potential. Once again, $F^{(22)}$ is much larger than $F^{(21)}$ for the same reason discussed above. The second-order force is a much bigger or even a dominant component in the total force as shown in Fig. 21, compared with those results at $k_0a = 1.66$. The free surface wave

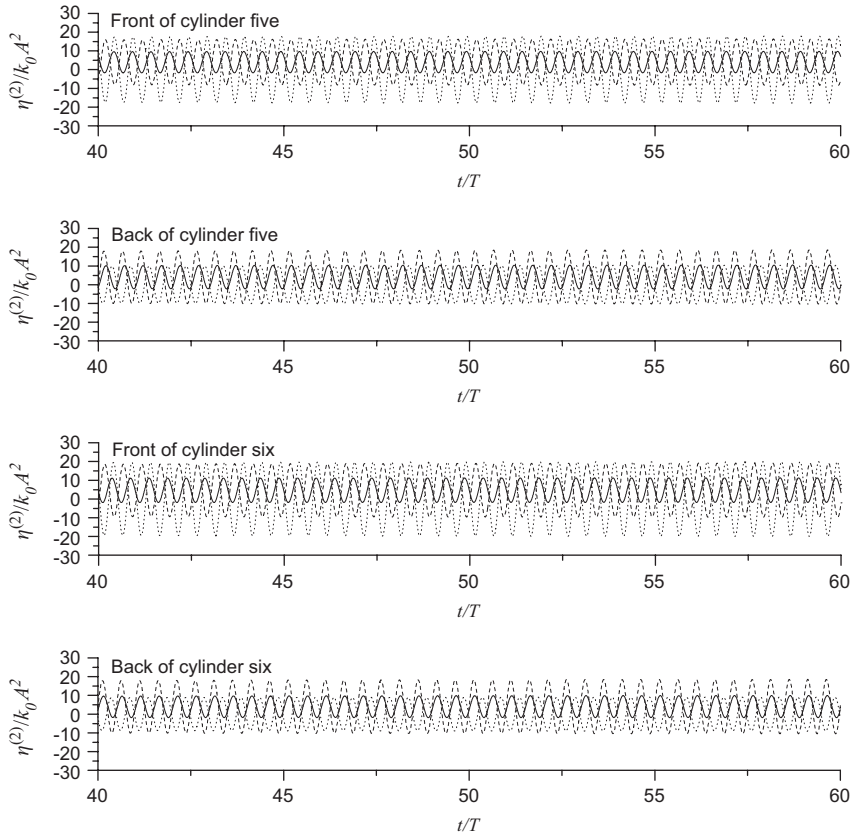

Fig. 30. Second-order waves and components for cylinders 5 and 6. Dash line: $\eta^{(21)}$; Dot line: $\eta^{(22)}$; Solid line: $\eta^{(2)}$.

profiles around the cylinders at $k_0a = 0.468$ are shown in Fig. 22. The inclusion of second-order component has changed the wave pattern completely.

To demonstrate the flexibility of the present numerical procedure, we next consider truncated cylinders in the same configuration as that in Fig. 14. The cylinders all have the identical draught $d = 0.5\,h$ and $L_{cy} = 4a$. The wave history at $k_0a = 1.66$ is given in Fig. 23 for cylinder 1 and Fig. 24 for cylinder 3. The results are hardly different from those for the bottom mounted cylinders. This is expected, as the main component in this case is the linear one and the major action of the linear wave at this frequency is near the free surface. The change near the seabed usually does not affect too much the results near the free surface. Figs. 25 and 26 give waves for cylinder 3 at $k_0a = 0.468$. The difference between wave run-ups for the bottom mounted cylinder and the truncated cylinder becomes more evident as the disturbance decays more slowly along the depth at lower frequency. A big difference can be seen in the second-order waves. This is because the second-order potential decays much more slowly than the first-order one along the depth, which was observed by Eatock Taylor et al. (1989) and then discussed in detail by Newman (1990). The forces on truncated cylinder 3 at $k_0a = 0.468$ are given in Fig. 27. They show the highly significant effect of the second-order component. Another difference between the truncated cylinder and the bottom mounted cylinder is that there is a vertical force on the former, which is also included in the figures.

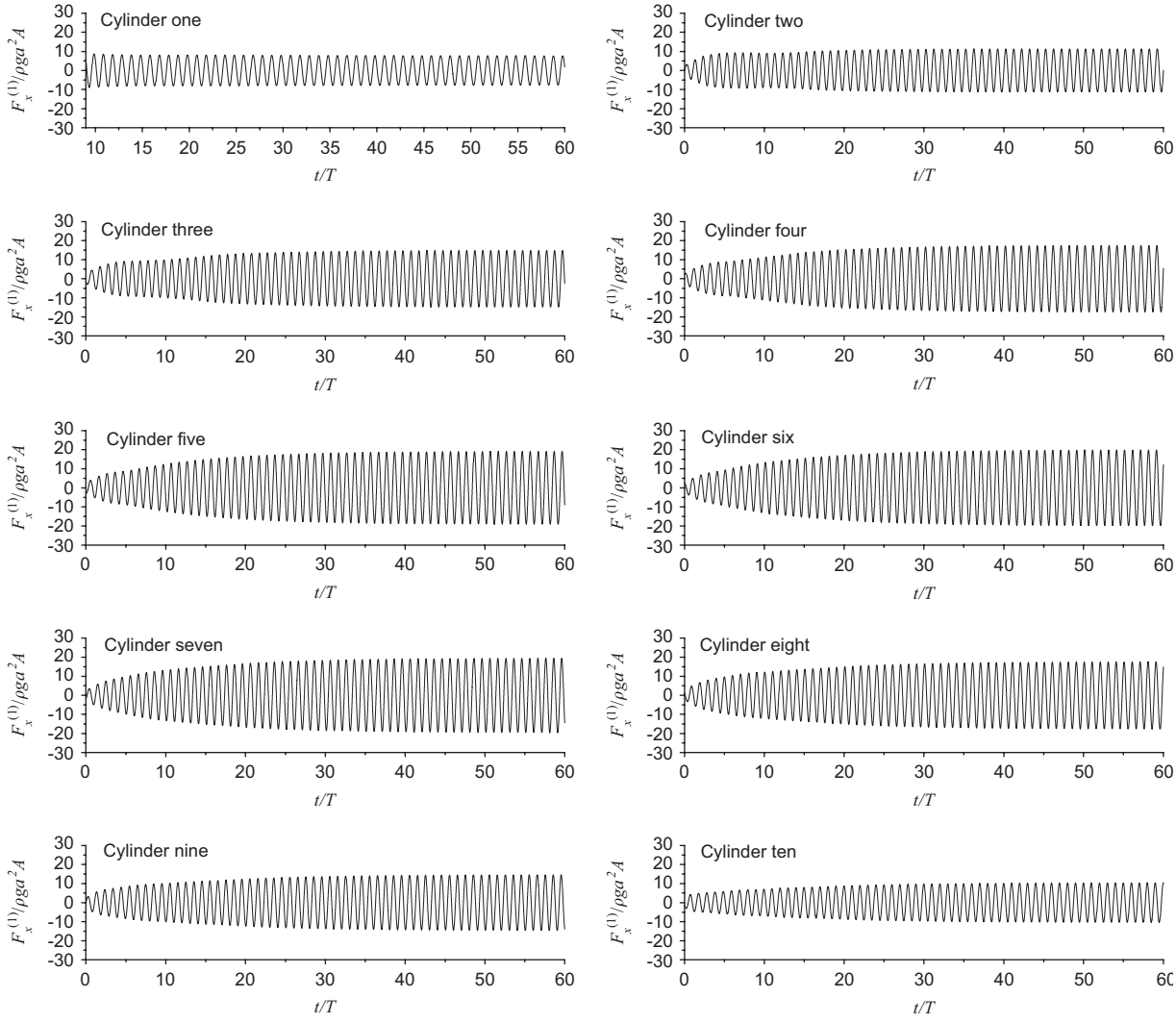

Fig. 31. Histories of linear forces on the 10 cylinders.

4.3. An array of cylinders

The results for a 10-cylinder case shown in Fig. 28 are given in Figs. 29–32. The 10 cylinders are placed along the line $y = 0$ with an identical distance L_{cy} between two adjacent bodies. The configuration is symmetric about $x = 0$. In the simulation, $L_{cy} = 4a$ and $k_0a = 0.673$ which is near the Neumann trapped mode given by Maniar and Newman (1997). The wave run-ups along the two cylinders at two ends and two cylinders in the middle are given in Fig. 29. It can be seen that the result corresponding to cylinders 5 and 6 are larger than those corresponding to 1 and 2. This is consistent with the linear results of Maniar and Newman (1997) from the frequency domain method. Fig. 30 gives the second-order wave elevation. As in the four cylinder case, the components may be big but the total result is much smaller due to cancellation. Fig. 31 gives the forces on all the cylinders. The general trend is again that towards the middle the force becomes bigger. It can be seen that the envelope of the amplitude evolves very slowly and will stabilize after many periods, which is similar to the behaviour in Fig. 17. Wave profiles at $t = 25T$ are given in Fig. 32, in which the contribution from the second-order component is quite obvious.

The diffraction by eight truncated cylinders in double lines with $d = 0.5\,h$ shown in Fig. 33 is also simulated. This case resembles the columns of a floating airport, although the total number of 8 is relatively low. The distance between two neighbouring cylinders is $L_{cy} = 4a$ and the distance between two columns is also $4a$. We provide results for cylinders 1,2,3 and 4 only, because of symmetry. The waves at $k_0a = 0.456$ are given in Figs. 34 and 35. Generally, the waves at the front sides of cylinders are larger than those on their back sides. Nonlinearities at the front sides of these cylinders

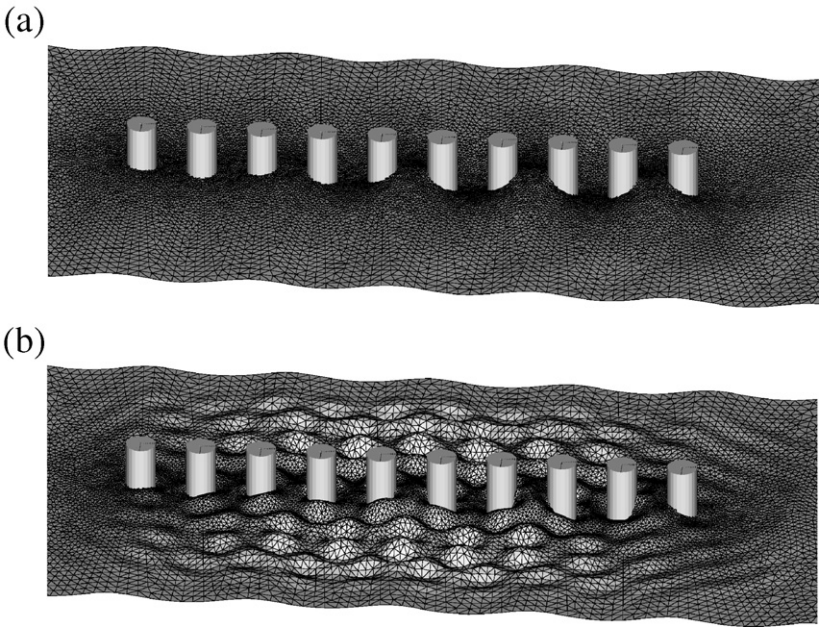

Fig. 32. Free surface profiles at $t = 25T$: (a) linear; (b) linear plus second order.

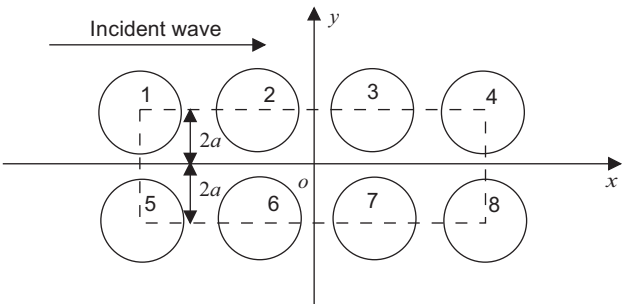

Fig. 33. Eight-cylinder case.

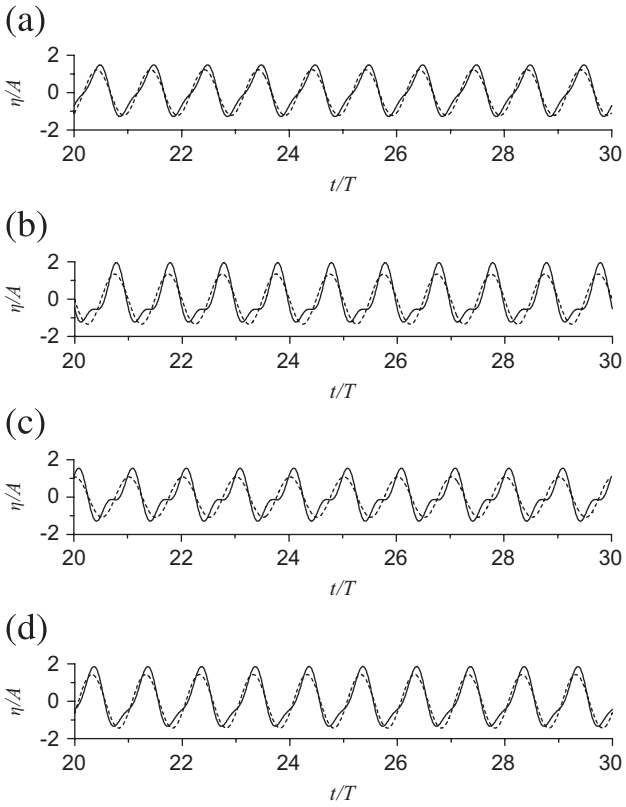

Fig. 34. Histories of waves at the fronts of cylinders (a) 1, (b) 2, (c) 3, (d) 4. Dash line: linear; Solid line: linear plus second order.

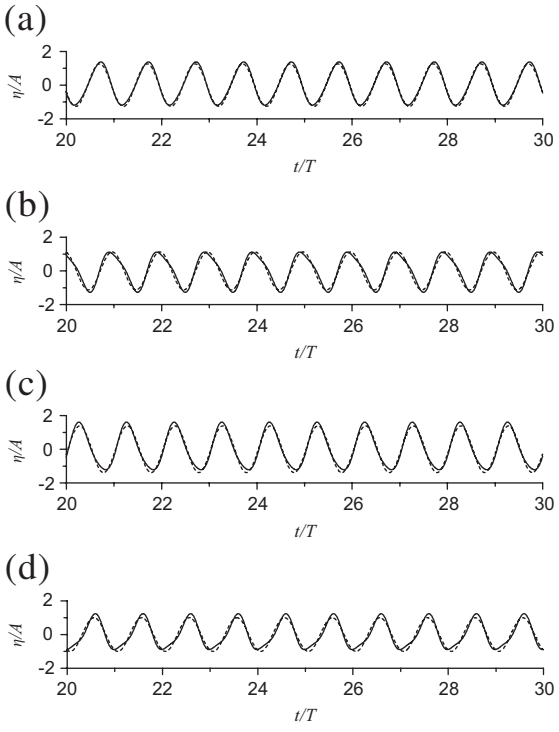

Fig. 35. Histories of waves at the backs of cylinders (a) 1, (b) 2, (c) 3, (d) 4. Dash line: linear; Solid line: linear plus second order.

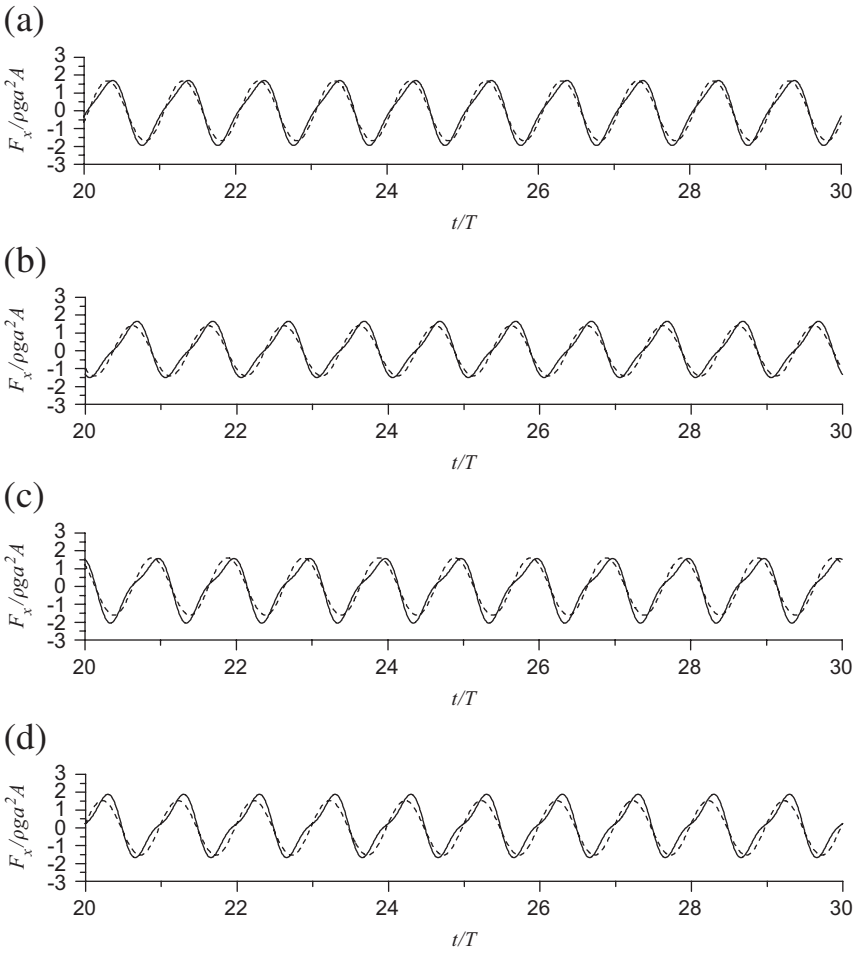

Fig. 36. Histories of forces on cylinders (a) 1, (b) 2, (c) 3 and (d) 4. Dash line: linear; Solid line: linear plus second order.

are also stronger, and the amplitude of the second-order wave is about 44.6% that of the first-order for cylinder 2 while it is 53% for cylinder 3. The forces F_x and F_z are given in Figs. 36 and 37, while F_y has been ignored as it is small. A snapshot of the wave provide for this case at $t = 25\,T$ are shown in Fig. 38.

5. Conclusions

A finite-element-based time domain method has been used to analyse second-order wave diffraction by a group or an array of cylinders. Extensive simulations have been made for a variety of configurations of cylinders. The results obtained are consistent with those from the frequency domain analysis. The effects due to interactions are well captured, in particular the behaviour near the trapped mode. It is observed that the transition to the periodic state for multi-cylinders takes much longer than that for a single cylinder. When the wavenumber is near the trapped mode, the evolution of the envelopes of the force and wave amplitudes can be very slow.

Although many of the cases simulated in this paper have been considered previously in the frequency domain, the present method offers a far greater potential. The simulation does not have to be limited to the periodic case. The method can be used for arbitrarily transient waves or waves with many periodic components. Furthermore, the use of the finite element method means that it is possible to simulate cases corresponding to more complicated shapes, other than circular cylinders. All these are of course based on the assumption that the perturbation method is valid.

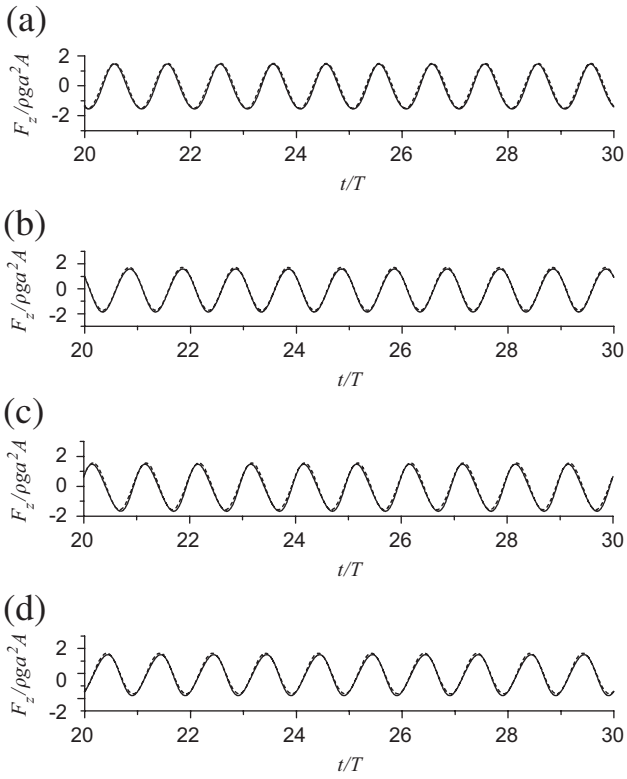

Fig. 37. Histories of forces on cylinders (a) 1, (b) 2, (c) 3 and (d) 4. Dash line: linear; Solid line: linear plus second order.

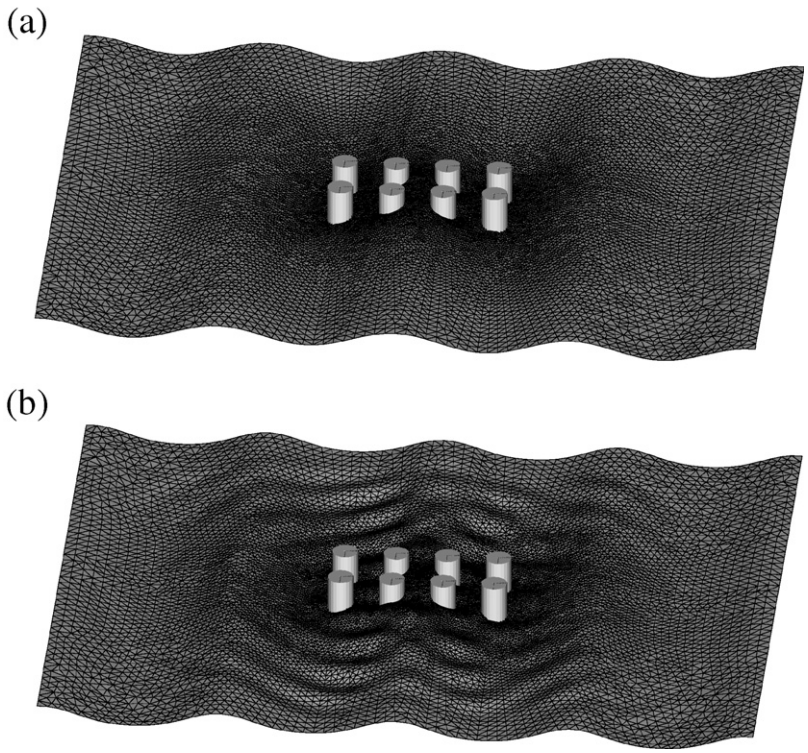

Fig. 38. Free surface profiles at $t = 25T$. (a) linear (b) linear plus second order.

References

Abul-Azm, A.G., Williams, A.N., 1988. Second order diffraction loads on truncated cylinders. ASCE Journal of Waterway, Port, Coastal and Ocean Engineering 114, 436–454.

Beck, R.F., Liapis, S.J., 1987. Transient motions of floating bodies at zero forward speed. Journal of Ship Research 31, 164–176.

Chau, F.P., 1989. The second order velocity potential for diffraction of waves by fixed offshore structures. Ph.D. Thesis, Department of Mechanical Engineering, University College London.

Chau, F.P., Eatock Taylor, R., 1992. Second-order wave diffraction by a vertical cylinder. Journal of Fluid Mechanics 240, 571–599.

Chung, T.J., 2002. Computational Fluid Dynamics. Cambridge University Press.

Eatock Taylor, R., Hung, S.M., 1987. Second order diffraction force on a vertical cylinder in regular waves. Applied Ocean Research 9, 19–31.

Eatock Taylor, R., Hung, S.M., Chau, F.P., 1989. On the distribution of second order pressure on a vertical circular cylinder. Applied Ocean Research 11, 183–193.

Evans, D.V., Porter, R., 1997a. Trapped modes about multiple cylinders in a channel. Journal of Fluid Mechanics 339, 331–356.

Evans, D.V., Porter, R., 1997b. Near-trapping of waves by circular arrays of vertical cylinders. Applied Ocean Research 19, 83–99.

Hecht, F., 1998. BAMG: Bidimensional anisotropic mesh generator. Website: http://www-rocq1.inria.fr/gamma/cdrom/www/bamg/eng.htm.

Hu, P.X., Wu, G.X., Ma, Q.W., 2002. Numerical simulation of nonlinear wave radiation by a moving vertical cylinder. Ocean Engineering 29, 1733–1750.

Isaacson, M., Cheung, K.F., 1990. Time-domain solution for second-order wave diffraction. ASCE Journal of Waterway, Port, Coastal and Ocean Engineering 116, 191–210.

Isaacson, M., Cheung, K.F., 1991. Second order wave diffraction around two-dimensional bodies by time-domain method. Applied Ocean Research 13, 175–186.

Isaacson, M., Cheung, K.F., 1992. Time-domain second-order wave diffraction in three dimensions. ASCE Journal of Waterway, Port, Coastal and Ocean Engineering 118, 496–516.

Kashiwagi, M., Ohwatari, Y., 2002. First- and second-order water waves around an array of floating vertical cylinders. 17th International Workshop on Water Waves and Floating Bodies, Cambridge, UK.

Kim, M.H., Yue, D.K.P., 1989. The complete second-order diffraction solution for anaxisymmetric body, Part II. Bichromatic incident waves. Journal of Fluid Mechanics 200, 235–264.

Lighthill, M.J., 1979. Waves and hydrodynamic loading. Proceedings of second International Conference on the Behaviour of Offshore Structures, London, pp. 1–40.

Ma, Q.W., Wu, G.X., Eatock Taylor, R., 2001a. Finite element simulation of fully nonlinear interaction between vertical cylinders and steep waves. Part 1: Methodology and numerical procedure. International Journal for Numerical Methods in Fluids 36, 265–285.

Ma, Q.W., Wu, G.X., Eatock Taylor, R., 2001b. Finite element simulation of fully nonlinear interaction between vertical cylinders and steep waves. Part 2: Numerical results and validation. International Journal for Numerical Methods in Fluids 36, 287–308.

Malenica, S., Eatock Taylor, R., Huang, J.B., 1999. Second order water wave diffraction by an array of vertical cylinders. Journal of Fluid Mechanics 390, 349–373.

Maniar, H.D., Newman, J.N., 1997. Wave diffraction by a long array of cylinders. Journal of Fluid Mechanics 339, 309–330.

Molin, B., 1979. Second order diffraction loads upon three-dimension bodies. Applied Ocean Research 1, 197–202.

Molin, B., Marion, A., 1986. Second order loads and motions for floating bodies in regular waves. Proceedings of Offshore Mechanics and Arctic Engineering Conferrence, Tokyo, pp. 353–360.

Nakos, D.E., Kring, D., Sclavounos, P.D., 1993. Rankine panel methods for transient free surface flows. Sixth International Conference on Numerical Ship Hydrodynamics, Iowa.

Newman, J.N., 1990. Second-harmonic wave diffraction at large depths. Journal of Fluid Mechanics 213, 59–70.

Ohl, C.O.G., Eatock Taylor, R., Taylor, P.H., Borthwick, A.G.L., 2001. Water wave diffraction by a cylinder array. Part 1. Regular waves. Journal of Fluid Mechanics 442, 1–32.

Pawlovski, J., 1992. A nonlinear theory of ship motion in waves. Proceedings of 19th Symposium on Naval. Hydrodynamics, Seoul.

Ursell, F., 1951. Trapping modes in the theory of surface waves. Proceedings of the Cambridge Philosophical Society 47, 347–358.

Vada, T., 1987. A numerical solution of second-order wave-diffraction problem for submerged cylinder of arbitrary shape. Journal of Fluid. Mechanics 174, 23–37.

Wang, C.Z., Wu, G.X., 2006. An unstructured mesh based finite element simulation of wave interactions with non-wall-sided bodies. Journal of Fluids and Structures 22, 441–461.

Wu, G.X., 1991. On second order wave reflection and transmission by a horizontal cylinder. Applied Ocean Research 13, 58–62.

Wu, G.X., Eatock Taylor, R., 1990. Second order diffraction forces on horizontal cylinders in finite water depth. Applied Ocean Research 12, 106–111.

Wu, G.X., Eatock Taylor, R., 1995. Time stepping solutions of the two dimensional nonlinear wave radiation problem. Ocean Engineering 22, 785–798.

Wu, G.X., Hu, Z.Z., 2004. Simulation of nonlinear interactions between waves and floating bodies through a finite element based numerical tank. Proceedings of the Royal Society London A 460, 2797–2817.

Wu, G.X., Ma, Q.W., Eatock Taylor, R., 1998. Numerical simulation of sloshing waves in a 3D tank based on a finite element method. Applied Ocean Research 20, 337–355.